Natural fracture patterns at Swift anticline, NW Montana: the influence of structural position and lithology from multiple observation scales

5 Adam J. Cawood[1,a], Hannah Watkins[1], Clare E. Bond[1], Marian J. Warren[2], Mark A. Cooper[1,3]

[1] School of Geosciences, University of Aberdeen, King's College, Aberdeen AB24 3UE, UK
[2] Jenner GeoConsulting Inc., 107 Lake Tahoe Place SE, Calgary, Alberta, T2J 4B7, Canada
[3] Sherwood GeoConsulting Inc., 140 Lake Mead Cr SE, Calgary, Alberta, T2J 4A1, Canada
10 [a] Present address: Southwest Research Institute, 6220 Culebra Rd, San Antonio, Texas 78238-5166, USA

Correspondence to: Adam J. Cawood (adam.cawood@swri.org)

Abstract. Natural fracture patterns have long been associated with fold formation. Conceptual models of fold associated fractures are used to predict fracture networks and hence subsurface properties such as fracture connectivity, intensity and fluid flow. Subsurface datasets typically lack the resolution or coverage to adequately sample fracture networks in 3D, 15 however, and geometric properties are typically extrapolated from available data (e.g., seismic data or wellbore image logs). Here we assess the applicability of extrapolating fracture properties (orientation, length and intensity) from one observation scale to another on a contractional anticline and assess the interplay of fracture scaling with geological controls on fracture development. Fracture patterns are investigated at an outcrop exposure of layered carbonate rocks at Swift anticline, NW Montana. Data derived from high-resolution field images, medium resolution digital outcrop data, and relatively low resolution 20 satellite imagery are leveraged to (i) assess interacting structural and stratigraphic controls on fracture development, and (ii) compare estimated fracture properties derived from multiple observation scales. We show that hinge-parallel and hinge-perpendicular fractures (i) make up the majority of fractures at the site, (ii) are consistently oriented with respect to the fold hinge despite along-strike variability in the fold hinge orientation, and (iii) exhibit systematic increases in intensity towards the anticline hinge. These fractures are interpreted as having formed during folding. Other fractures recorded at the site exhibit 25 inconsistent orientations, show no systematic trends in fracture intensity, and are interpreted as unrelated to fold formation. Fracture orientation data exhibit greatest agreement across observation scales at hinge and forelimb positions where hinge-parallel and hinge-perpendicular fracture sets are well developed, and little agreement on the anticline backlimb, where fracture orientations are less predictable and more dispersed. This indicates that the scaling of fracture properties at Swift anticline is spatially variable and partly dependent on structural position. Our results suggest that accurate prediction and extrapolation of 30 natural fracture properties in contractional settings requires assessment of structural position, lithologic variability, and spatially variable fracture scaling relationships, as well as consideration of deformation history before and after folding.
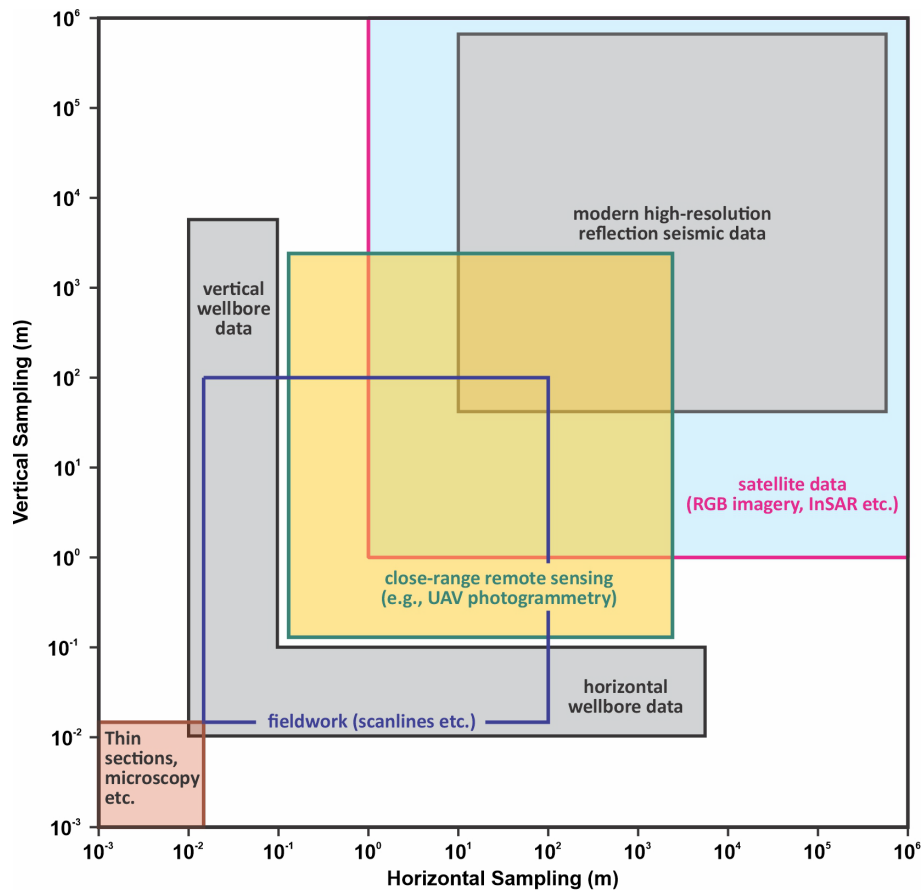
1 Introduction

The ability to predict accurately natural fracture attributes (e.g., aperture, length, orientation) and patterns (e.g., density, connectivity) has implications for resource management and waste disposal in the subsurface. Natural fractures typically enhance the porosity and permeability of subsurface rock volumes and predicting fracture attributes is therefore important for a range of activities related to subsurface fluid flow regimes. Specific applications include CO_2 sequestration (e.g., Iding and Ringrose, 2010; Bond et al., 2013, 2017; Gholami et al., 2021; Kou et al., 2021), hazardous waste disposal (e.g., Green and Mair, 1983; Gautschi, 2001; Morris et al., 2004; Yu et al., 2021; Ishii, 2022), groundwater management (e.g., Streltsova, 1976; Bachu, 1995; Ferrill et al., 1999; Medici et al., 2021; Moore and Walsh, 2021), hydrocarbon extraction (e.g., Thomas et al., 1983; Mäkel, 2007; Rawnsley et al., 2007; Li and Lee, 2008; Spence et al., 2014; Gong et al., 2021) and geothermal energy production (e.g., Bödvarsson and Tsang, 1982; Watanabe and Takajashi, 1995; Shaik et al., 2011; Fox et al., 2013; Glaas et al., 2021; Chabani et al., 2022). Despite the range of applications that rely on knowledge of subsurface fracture properties, accurate fracture prediction remains challenging due to (i) the spatial variability and complexity of natural fracture networks, and (ii) difficulties related to sampling fracture populations in subsurface datasets.

Subsurface data (e.g., wellbore information and seismic imaging) provide constraints on fracture properties, but limits to the coverage and resolution of these datasets often result in highly uncertain predictions of fracture properties at depth. Wellbore data can provide direct, in-situ fracture measurements (e.g., orientation data from image logs) which can be used for generating predictive fracture models (e.g., Cooper, 1991; Aliverti et al., 2003; Nadimi et al., 2020). Wellbores are generally widely spaced in the subsurface, however, and predictions from well data typically suffer from sampling biases (e.g., Sun et al., 2016; Yin and Chen, 2020). Extrapolating fracture properties (e.g., length, orientation, abundance) away from wells or interpolating between wells is therefore not straightforward, with predictions prone to substantial uncertainties (e.g., De Marsily, 2005; Ma et al., 2007). Remote sensing (e.g., seismic reflection) data provide a potential alternative for sampling subsurface fracture populations but these data typically lack the resolution to image all but the largest fractures or discontinuities in the subsurface (e.g., Marrett and Allmendinger, 1992; Yielding et al., 1996; Rawnsley et al., 2007; Worthington & Lubbe, 2007; Dimmen et al., 2023). As such, seismic data are generally more useful for providing contextual information (e.g., structural position, distance to major faults) than for directly imaging fracture networks in detail.
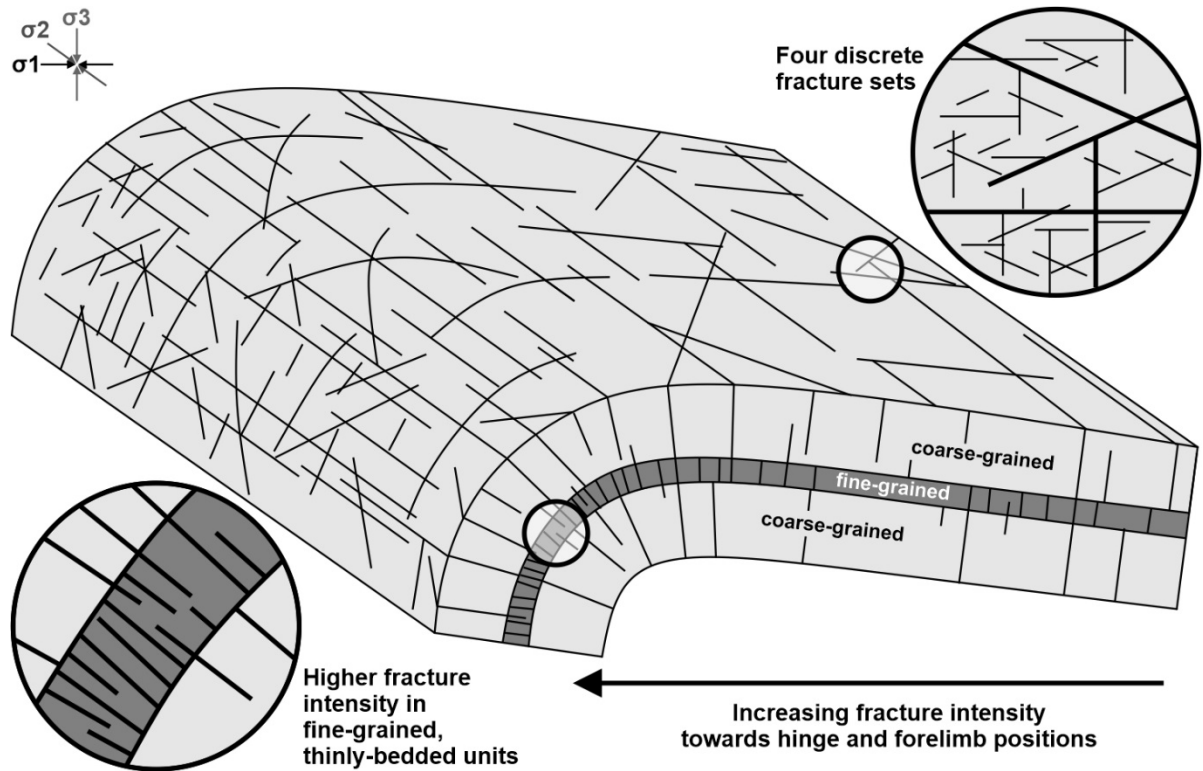
Faced with limited information about subsurface fracture properties, geoscientists may supplement subsurface datasets with information derived from appropriate outcrop analogues (e.g., Inks et al., 2015; Becker et al., 2018; Ukar et al., 2019). Recent advances in digital photogrammetry and digital mapping approaches (e.g., James and Robson, 2012; Cawood et al., 2017, 2022; Corradetti et al., 2018; Bowness et al., 2022) provide the opportunity to map and measure fractures at outcrop across a range of spatial scales (e.g., Strijker et al., 2012; Seers and Hodgetts, 2014; Hardebol et al., 2015). By integrating traditional fieldwork with modern digital approaches, fracture characterization at outcrop can potentially (i) address sampling gaps in subsurface datasets (Fig. 1), and (ii) be leveraged to generate multi-scale predictions of inherently heterogeneous fracture populations (e.g., Vollgger and Cruden, 2016; Smeraglia et al., 2021).

65   While these represent major improvements in our ability to map fractures, it should be noted that not all fractures at outcrop are not necessarily representative of those in the subsurface. Fracture formation can be driven by various surface and subsurface processes such as weathering, topographic stresses, and pore fluid pressure changes (e.g., Ukar et al., 2019 and references therein) and therefore outcrops may exhibit higher fracture abundances than equivalent subsurface rocks. Conversely, sampling of fracture networks at outcrop may be hampered by imperfect exposure. Swift anticline, like many

70   outcrops, is partially vegetated and parts of the exposure have been removed by erosion – we acknowledge that this may impact our results but leverage all available exposures at the site for this study. Finally, improved sampling of fracture networks does not necessarily lead to a better understanding of fracture mechanisms and timing (see Laubach et al., 2019 for a detailed review of this topic). By leveraging field measurements, close-range remote sensing data, and satellite imagery to characterize fracture patterns at a range of scales, in multiple lithologies, and at different structural positions, the aim of this study is to overcome

75   some of the non-uniqueness of outcrop-based fracture interpretation studies.

Figure 1: Scale of geological datasets at which natural fracture networks are typically characterized. Filled grey boxes represent subsurface datasets; unfilled boxes are other data types. The approximate sampling scale for fieldwork refers to the scale at which fracture patterns can be comprehensively sampled using traditional field methods such as fracture scanlines or sampling windows.

3

The controls on fracture properties in folded sedimentary rocks have been investigated by numerous workers. Early conceptual models of fracture development predict the presence of discrete, systematic fracture sets on contractional anticlines (Fig. 2), where fracture orientations are kinematically consistent with the orientation of the fold on which they occur (e.g.,

85 Price, 1966; Stearns, 1964, 1969; Stearns and Friedman, 1972; Hancock, 1985). Subsequent studies have shown that these relatively simple conceptual relationships may be modified by a range of lithological, mechanical, and structural factors (e.g., Cosgrove and Ameen, 1999; Cooper et al., 2006; Wennberg et al., 2007; Bergbauer and Pollard, 2004; Watkins et al., 2015, 2018; Awdal et al., 2016). Documented lithological influences on fracture formation include rock competence (e.g., McGinnis et al., 2017; Bowness et al., 2022), grain size or porosity within units (e.g., Hanks et al., 1997; Wennberg et al., 2006),

90 mechanical layer thickness (e.g., Ladeira and Price, 1981; Narr and Suppe, 1991; Wu and Pollard, 1995), and bed interface characteristics (e.g., Cooke and Underwood, 2001; Cooke et al., 2006; McGinnis et al., 2017), among other factors.

Figure 2: Conceptual diagram showing established relationships between geological properties and fracture attributes in folded
95 **sedimentary rocks. Depicted relationships are: (i) increased fracture intensities at hinge proximal or high curvature zones, (ii) higher fracture intensities in fine-grained or thinly bedded carbonate lithologies, and (iii) the presence of four discrete fracture sets on contractional anticlines. Based on conceptual models by several authors (e.g., Price, 1966; Stearns, 1964, 1969; Stearns and Friedman, 1972; Hancock, 1985; Watkins et al., 2015, 2019)**

100 Structural controls on fracture attributes include proximity to faults (e.g., Caine et al., 1996; Tamagawa & Pollard, 2008; McGinnis et al., 2015), structural position on folds (e.g., Harris et al., 1960; Hennings et al., 2000; Watkins et al., 2015, 2018) and fold curvature in both dip and strike directions (e.g., Lisle 1992, 1994; Fischer and Wilkerson, 2000). Regional or local

stresses and stress perturbations (e.g., Hancock 1985; Tamagawa and Pollard, 2008; Ferrill et al., 1999), burial history and progressive diagenesis (e.g., Laubach et al., 2009; Hooker et al., 2013), and previous episodes of deformation (e.g., Agosta et al., 2010; Casini et al., 2011; Ferrill et al., 2021) are among some of the other factors that may influence fracture network properties. Each of the relationships outlined above may impart spatial variability to natural fracture networks and as a result, fracture properties may vary both in 3D and across spatial scales (e.g., Gillespie et al., 1993, 2001; Castaing et al., 1996; Odling, 1997; Bonnet et al., 2001; Bossennec et al., 2021).

Here we combine 3D photogrammetric reconstruction techniques with field-based measurements and Google Earth imagery to perform a multiscale assessment of fracture properties at Swift anticline, NW Montana. We assess (i) the link between lithology (grain size, rock texture) and fracture intensity, (ii) the influence of structural position vs. fracture orientations and fracture intensity, and (iii) the effects of observation scale on estimated fracture properties. We show that stratigraphic exposure level influences fracture intensity irrespective of structural position but that only fracture sets oriented parallel and perpendicular to the fold exhibit increases in fracture intensity towards the fold hinge. By characterizing structural and stratigraphic controls on fracture development at multiple observation scales, we provide insights into the scale dependence of fracture formation in deformed multilayer systems.

2 Geological Setting

The Sawtooth Range is a NNW-SSE trending fold-thrust belt that marks the eastern edge of the Rocky Mountains in NW Montana (Fig. 3A, B). Cambrian through Cretaceous stratigraphy is deformed and exposed in the Sawtooth Range (Fig. 3C, D). This belt of exposed thrusts and related folds is bound to the west by the Lewis-Eldorado Thrust system and to the east by Jurassic-Paleogene foreland basin deposits associated with the Cordilleran Orogeny (Fuentes et al., 2012). The main phase of fold-thrust deformation in the Sawtooth Range is interpreted to have occurred during late Cretaceous to Palaeocene (Fuentes et al., 2012). Thrusts within the Sawtooth Range are generally closely-spaced, laterally continuous, and westward dipping, and exhibit a general trend for increased dips westwards, towards the hinterland (Fig. 3C, D). The Sawtooth Range is interpreted as a thin-skinned deformation belt (Mudge, 1982; Mitra, 1986; Holl & Anastasio, 1992; Fuentes et al., 2012) and the stacked thrust sheets of the Sawtooth Range have been interpreted as an exhumed and eroded thrust duplex that formed below the overlying Lewis-Eldorado thrust (Ward & Sears, 2007).

Several studies have focused on fracture patterns within Mississippian carbonate rocks at localities in the Sawtooth Range. Early work by Stearns (1964, 1969) and by Stearns and Friedman (1972) focused on fracture orientations at Teton anticline (c. 35 km to the south of Swift anticline). This work led to the development of strategies for differentiating between shear vs. extension fractures on anticlines based on their orientations with respect to the fold hinge. The results of these studies led to the widespread use of general models for predicting fracture orientations on and around open folds (e.g., McQuillan, 1973; Fisher & Wilkerson, 2000; Cooper et al., 2006). Later work at Teton anticline focused on fracture spacing (Sinclair, 1980) and the effects of curvature (Spooner, 1984) and structural evolution (Ghosh & Mitra, 2009; Burberry et al., 2019) on
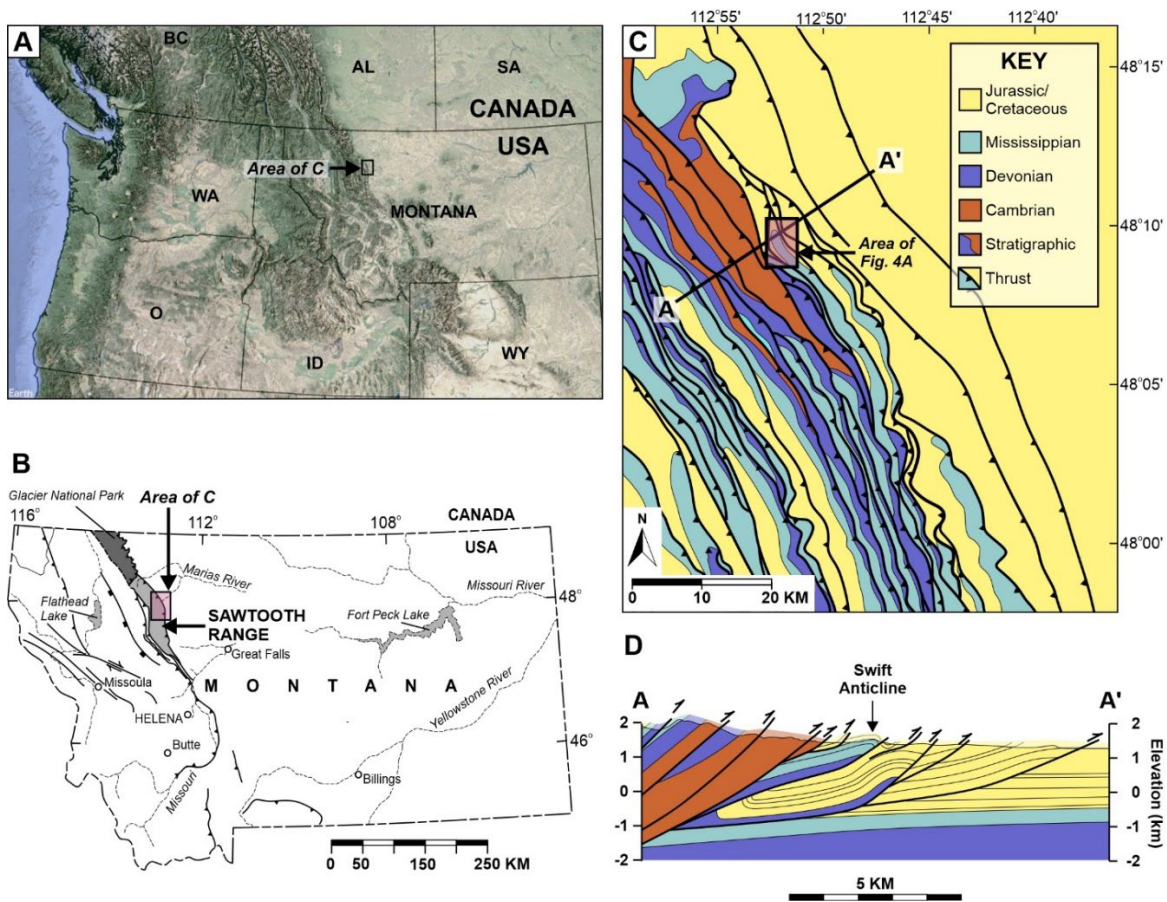
135   fracture attributes. Studies at Swift anticline have related fracture properties at the site to a range of geological factors, including extension driven by flexural loading (Ward & Sears, 2007), variable lithological properties in exposed units (Watkins et al., 2019), and regional stress rotations (Singdahlsen, 1986). Swift anticline has also been used as a direct surface analogue for subsurface gas fields in the eastern Rockies at Waterton, southern Alberta, Canada (Rawnsley et al., 2007).

3 Study Area

140   Swift anticline lies at the eastern edge of Swift Reservoir, NW Montana (Fig. 4A). The present-day erosion level across the anticline exposes carbonates of the Dupuyer Creek Unit (Nichols, 1984, 1986), of the upper part of the Mississippian Castle Reef Formation (Madison Group). At isolated localities, unconformably overlying fine-grained clastic rocks of the Jurassic Ellis Group are preserved (e.g., Fig. 4B). The Mississippian to Jurassic unconformity is widespread across NW Montana & SW Alberta, and records non-deposition and/or erosion on a possible forebulge before initial deposition in the Cordilleran

145   foreland basin (Ward and Sears, 2007; Fuentes et al., 2012). The Dupuyer Creek Unit makes up most of the exposed strata at Swift anticline and records multiple cycles of carbonate deposition in a shallow water environment, from high-energy, open marine conditions to a tidally influenced interior ramp setting (Mudge, 1982). Strata within the Dupuyer Creek Unit display significant variability in both composition and texture (Watkins et al., 2019), as defined by cyclical variations in depositional environment (e.g., Nichols, 1984).
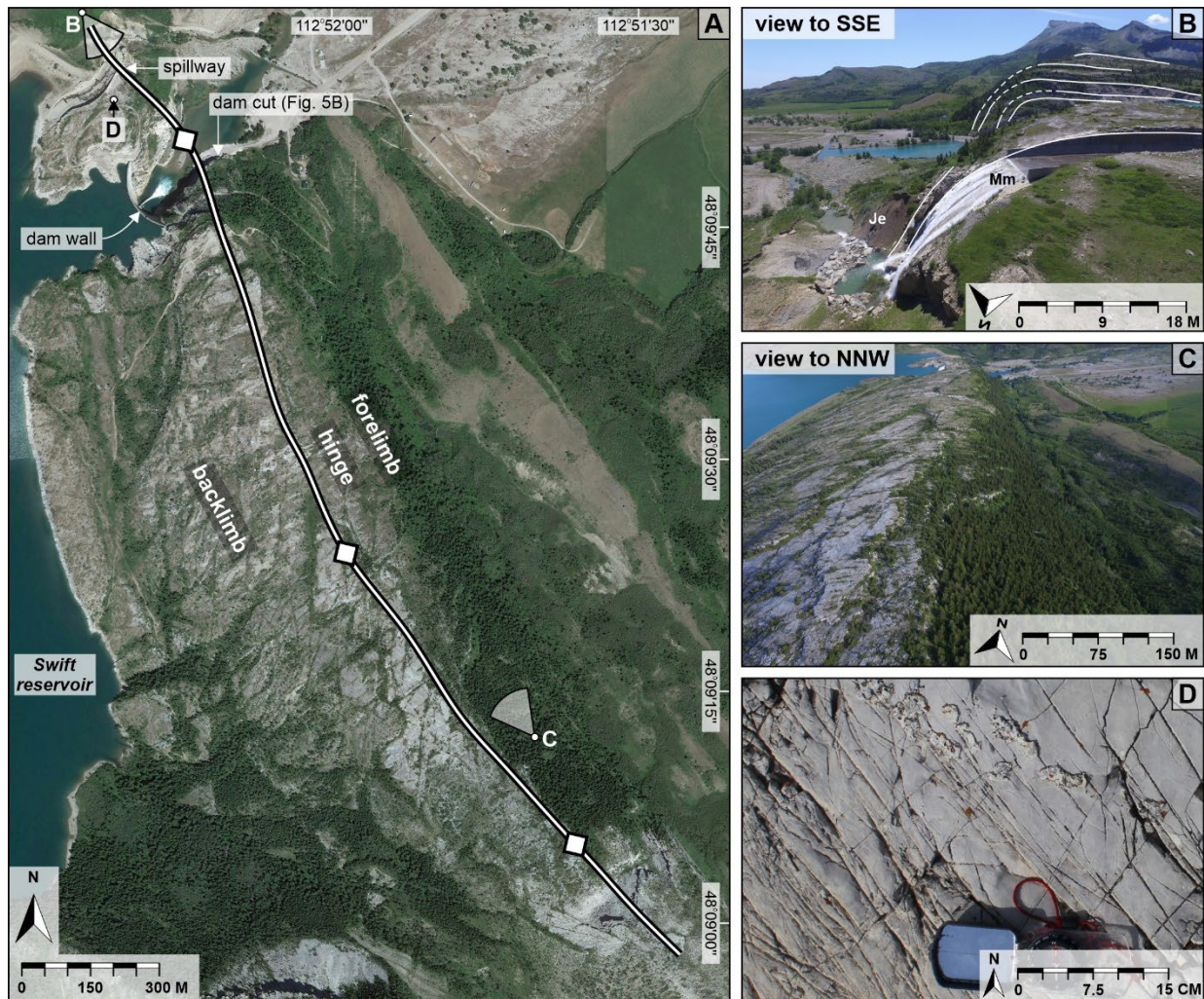
150   Swift anticline is situated in the footwall of an imbricate stack of thrust sheets involving primarily Cambrian to Devonian strata at outcrop (Fig. 3C). The fold is interpreted as a hanging-wall anticline above an ENE-verging thrust fault (Watkins et al., 2019), and is marked by a tight fold hinge with a narrow hinge zone (Watkins et al., 2019), and steeply dipping to overturned beds in the forelimb of the structure (Fig. 4B). The anticline trends NNW-SSE and is characterised by an arcuate axial trace, which records some variation in its orientation along the crest of the structure (Fig. 4A). The stepped erosional profile across

155   the crest of the structure (Fig. 4C) exposes several stratigraphic levels within the Dupuyer Creek Unit; the current erosion surface also includes a number of well exposed, areally extensive fractured bedding surfaces (e.g., Fig. 4D) at multiple along-strike locations and forelimb, hinge and backlimb positions. This extensive exposure of fractured bedding surfaces makes Swift anticline a suitable site to examine, at a range of scales, potential links and feedbacks between folding and fracturing in multi-layered carbonate stratigraphy.

160

Figure 3: Regional and geological context for Swift Anticline. (A) Regional overview map showing the location of the Sawtooth Range in NW Montana. Generated from satellite imagery (© Google Earth/Landsat/Copernicus) and regional elevation data (ASTER GDEM). (B) Enlarged map of Montana showing location of the Sawtooth Range and simplified structural configuration of the area, modified from Mudge (1982). (C) Simplified geological map for the central part of the Sawtooth Range, modified from Mudge (1982), Mudge & Earhart (1983), and Watkins et al. (2019). (D) Cross-section across Swift Anticline and surrounding area showing general structural geometries, modified from Watkins et al. (2019).

Figure 4: Multi-scale imagery of Swift Anticline. (A) Satellite image (© Google Earth/Landsat/Copernicus) showing large-scale, vegetated fractures on the crest of the structure. Ground pixel resolution = ca. 0.35 m. Annotations show locations and look directions for B, C, D, and approximate structural positions on the fold. **(B)** UAV acquired aerial image of Swift Anticline, looking to SSE along the crest of the structure. Swift Reservoir spillway, exposed fold forelimb and sub-Jurassic unconformity in the foreground of the image. Mm = Mississippian Madison Group; Je = Jurassic Ellis Group. **(C)** UAV acquired aerial image of the anticline, looking NNW along the crest of the structure. The stepped erosional profile along the anticline crest allows lithological boundaries to be mapped across the structure. **(D)** Field image of highly fractured coral boundstone unit exposed near the dam spillway.

4 Data and methods

Bedding, fault and fracture orientation measurements were collected at the study site using handheld analogue (Silva) and digital (FieldMove on iPad) compass clinometers. These data were used to characterize general structural geometries at

8

the site (e.g., bedding and fracture orientations), to ground-truth digitally-derived fracture orientations, and to supplement remotely acquired data. Sedimentary logging was carried out to capture variations grain size and rock texture through the exposed section. In addition to field-based measurements and observations, digital imagery was acquired at multiple scales at the site to assess scale dependent variations in fracture attributes. The position of the fold hinge is reproduced here using the results of Watkins et al. (2019), who conducted a curvature analysis and estimated the fold hinge position from bedding orientation data and a constructed 3D model of the top Castle Reef Formation.

Digital imagery and associated data at three observation scales were used for fracture characterization:

1. Satellite imagery (Google Earth, 2018) provided a large-scale, lower-resolution dataset, with an estimated ground-pixel resolution of 0.35 m over the study area. This imagery was used for preliminary digital mapping and generation of a large-scale, low-resolution fracture map.

2. 3D photogrammetric reconstruction of the study site was achieved through acquisition of low-altitude aerial imagery across the structure from 22 manually piloted UAV flights. These flights yielded 2987 aerial images, acquired at a range of altitudes (5-97 m) above the outcrop surface. Digital photogrammetric processing was carried out using Agisoft Photoscan Professional 1.6, according to established protocols (e.g., Bemis et al., 2014; Cawood et al., 2017) with 3D reconstructions oriented and scaled with GPS ground control points and calibrated against Google Earth imagery. This yielded a final photorealistic 3D mesh (digital outcrop) comprised of 2.9 million mesh triangle faces, with an average ground pixel resolution of 0.24 m and total coverage of ~ 1.5 km^2.

3. A total of 244 ground-based digital images, of sub-mm (0.1-0.3 mm) ground-pixel resolution, were collected at outcrop using a handheld DSLR camera during fieldwork. Handheld camera images used in this study for fracture orientation characterization were collected by Watkins et al. (2019) for fracture intensity analysis. Photographs of fractured bedding surfaces were acquired at a distance of 0.5 – 1.5 m from the outcrop, along a series of transects across the crest of the structure. Imagery was acquired along with GPS coordinates and camera orientation data at each photo location, allowing images to be georeferenced and re-oriented prior to manual digitisation of fracture traces.

Manual digitisation of fracture traces in 2D (satellite and ground-based images) and 3D (via digital outcrop) was performed in Move 2016.1 (formerly Midland Valley, now Petroleum Experts). Orientations of digitized fracture traces were extracted using FracPaQ 2.3 (Healy et al., 2017) and Move 2016.1. 2D fracture intensity was calculated from digitized fracture traces by calculating total fracture length per unit area in 2D [m/m^2]. Fracture intensity calculations were carried out in Move 2016.1 for handheld camera images and in ArcMap 10.5.1 (ESRI) for satellite and digital outcrop data. 3D polylines from digital outcrop mapping were projected onto a horizontal plane for orientation and intensity analysis. While this approach does not correct for bed dip and the effects of orientation and intensity distortion, it allows 2D satellite and 3D digital outcrop interpretations to be directly compared within equivalent reference frames. There is no straightforward way to account for geometric artefacts in satellite imagery (e.g., steeper beds may appear to have more closely-spaced fractures in the dip direction than is real) and therefore we elected to treat all fracture maps as essentially horizontal. While this may lead to overestimates of fracture intensity in fractures oriented perpendicular to the dip direction, we consider this effect to be relatively minor at the

scale of the analysis area. Note that most of the pavements exposed on the crest of Swift anticline have dips around 20° or less (Watkins et al., 2019) and therefore we expect the effects of intensity distortions to be relatively minor. We do not account for orientation distortions because we do not have a reliable method (using the remote sensing approach) for estimating the 3D orientation of fracture traces from polyline interpretations (either from satellite imagery or the 3D digital outcrop). Field images were interpreted in 2D with images oriented according to bed dip at each field station (i.e., images were rotated and scaled so that they had the same orientation as bedding). Fracture interpretations from field images were projected to a horizontal plane for intensity and orientation analysis. Again, while this may have introduced some minor geometric artefacts, this approach was taken so that consistency between datasets could be maintained.

The primary focus of this study is the extraction and analysis of fracture attributes from remote sensing data, with implications for extrapolating fracture properties across observation scales. As such, detailed observations of fracture morphology (e.g., fracture cements and kinematic indicators) are beyond the scope of this work. We refer the reader to Watkins et al. (2019) for detailed petrological analysis and descriptions of rock texture and mineralogy at Swift anticline.
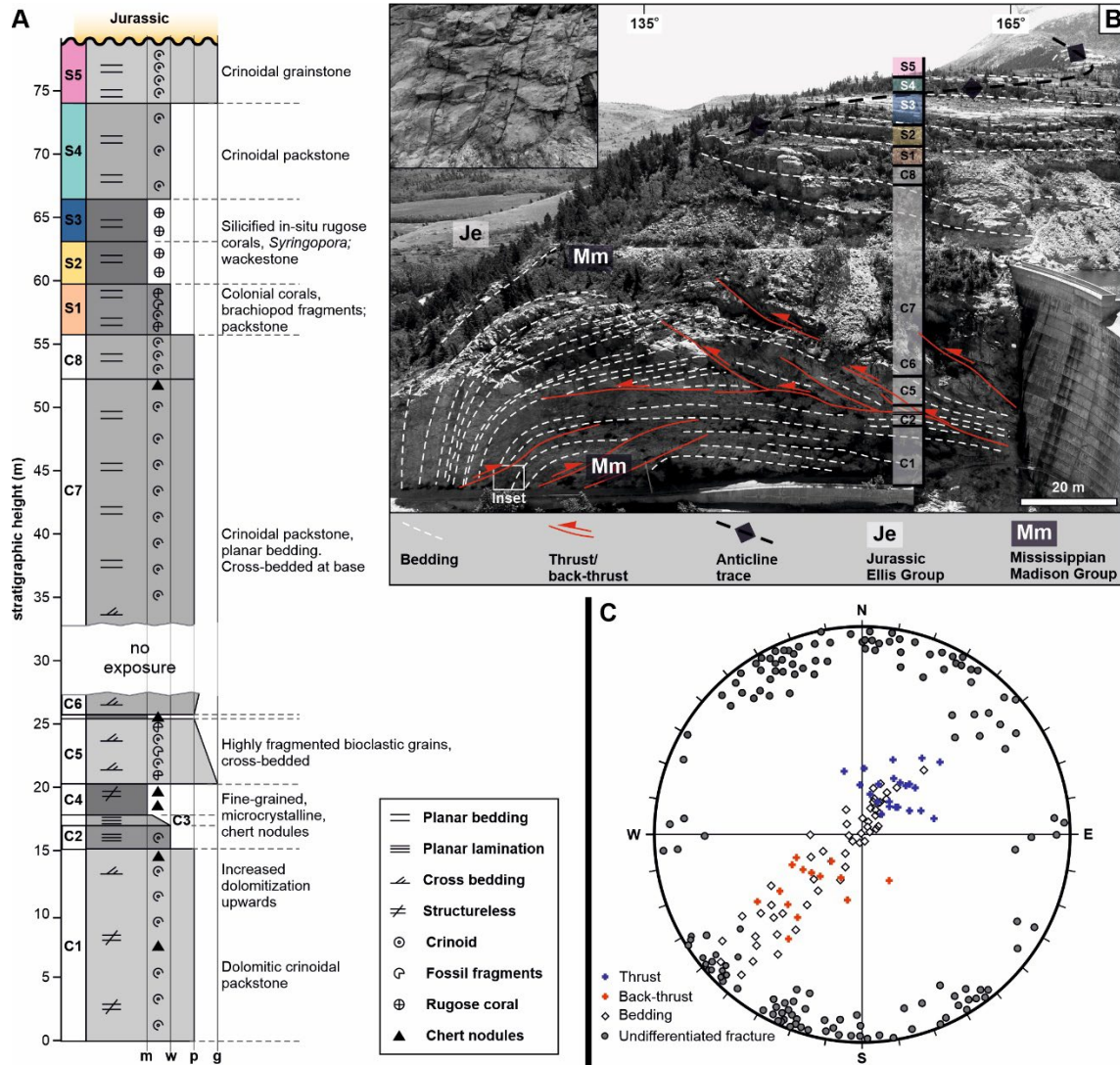

5 Results

5.1 Lithostratigraphy

Approximately 78 meters of distinctly bedded, partially dolomitized bioclastic limestones of the Dupuyer Creek Unit (Castle Reef Formation) is exposed in the dam-cut at Swift anticline (Figs. 5A, B). The exposed interval has been subdivided into several informal lithological units based on carbonate lithology and facies. Units C1-C8 are exposed in cross-section view only and overlying unit S1-S5 are exposed across the crest of the structure (Fig. 5A). Compositional and textural variations described by Watkins et al. (2019) in the exposed interval mainly reflect cyclical variations in depositional facies (e.g., Nichols, 1984). Bioclasts within coarse-grained units (grainstones and packstones) are dominated by dolomitized crinoid fragments. These grainstones and packstones are commonly structureless or marked by distinct planar cross-bedding (e.g., Unit C5; Fig. 5A). Fine-grained units (e.g., Units S2 & S3) are generally characterised by planar lamination, the presence of chert nodules, and microcrystalline textures. These mudstones or wackestones are generally mud-supported and commonly include large (several cm), isolated colonial corals, particularly in the upper part of the exposed section (Fig. 5A). Coarser-grained packstones and grainstones at Swift anticline generally record greater bed thicknesses (1.4 m – 18 m) than fine-grained wackestone lithologies (0.7 m – 2.6 m).

5.2 Fold geometry and field observations

A cross-sectional view of the anticline at Swift Reservoir dam (Fig. 5B) provides an overview of the fold geometry: the shallowly-dipping to horizontal backlimb transitions abruptly through a relatively narrow hinge zone to a steeply-dipping to vertical forelimb. Thrusts and back-thrusts, with relatively low offsets (> 0.5 m), are common through the exposed section (Fig. 5B). The cross-section view records a general trend for back-thrust dominance in the hinge and forelimb of the anticline,

250 with thrusts better developed in the backlimb of the structure. The fold geometry and thrust patterns may vary significantly through the structure; the dam cut cross-section, however, provides the best available cross-sectional view of Swift anticline.
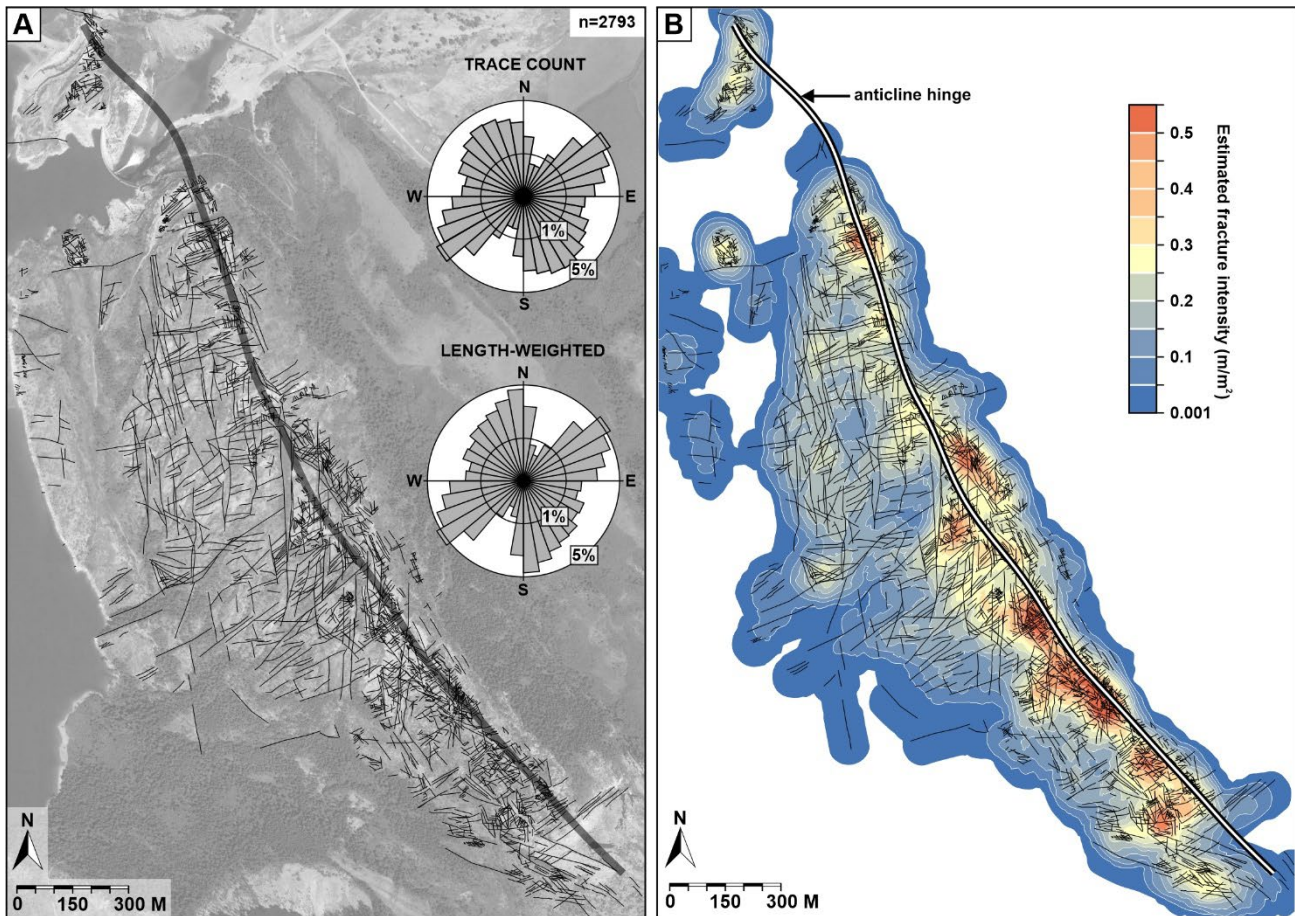
3D fracture orientations collected at the dam cut cross-section during fieldwork, and subsequently from a high-resolution digital outcrop of the same locality, record a range of fracture orientations (Fig. 5C). Most easily identified and measured at the dam cut cross-section are the thrusts and back-thrusts which typically have a strike orientation parallel to that of bedding,

255 with dips that range from sub-horizontal to ca. 50 degrees.

Figure 5: (A) Stratigraphic log through exposed units at the southern side of the Swift Reservoir dam cut. (B) Cross-sectional field image of dam cut showing general fold geometry, interpreted thrusts and back-thrusts, and approximate position of structural and
260 stratigraphic log in A. Note, units S1 to S5 defined as those exposed on the crest of the structure (see Fig. 10). C1 to C8 units exposed only in cross-section view in (B). Mm = Mississippian Madison Group; Je = Jurassic Ellis Group. (C) Orientation data from field and digital outcrop measurements showing NW-striking bedding planes, thrusts, back-thrusts and undifferentiated fractures. Fracture classifications in (C) based on field observations and fracture orientations.

11

5.3 Fracture attributes from Google Earth imagery

Fracture mapping of satellite imagery (0.3 – 0.4 m ground pixel resolution) was carried out using images downloaded from Google Earth. 2717 linear features were identified as fractures and digitized from satellite imagery (Fig. 6A). A rose plot of 2D fracture orientations by trace count (number of mapped fractures) record an approximately bimodal directional distribution with two dominant fracture sets oriented approximately parallel (NNW-SSE) and perpendicular (ENE-WSW) to the fold axial trace (Fig. 6A). A similar trend was reported from field-based measurements by Watkins et al. (2019).

Figure 6: (A) Manually interpreted fracture trace map from satellite imagery (© Google Earth/Landsat/Copernicus; pixel resolution = ca. 0.35 m). Rose plots show orientation distributions for all fractures mapped at this scale by fracture count (upper) and by cumulative length (lower). (B) Estimated 2D intensity (m/m²) of fractures mapped from satellite imagery. 2D fracture intensity calculated using the *Line Density* tool in *ArcMap 10.5.1* with 5 m grid cells and 50 m sampling window radii.

The length-weighted rose plot (histogram of summed lengths) of the same fracture traces (Fig. 6A) shows the greater lengths of N-S oriented fractures. Although the N-S fractures do not appear to make up a significant component of the fracture
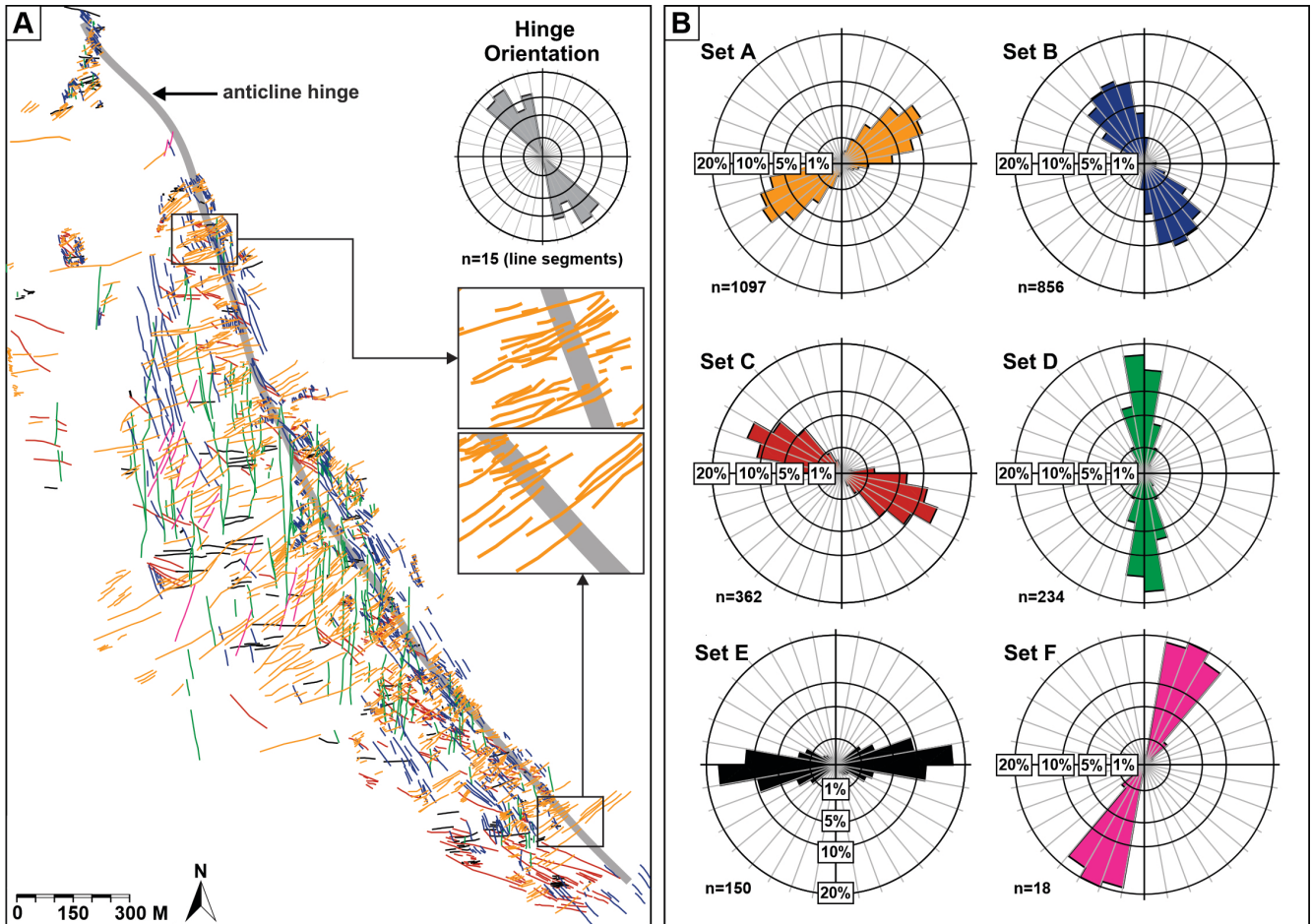
population by count, length-weighting the data shows the importance of these features as a contributor to the overall population. Bulk fracture intensities (total fracture length per unit area for all mapped fractures) from satellite image data show a general increase in fracture abundance towards the hinge zone of the anticline, particularly in central and southern domains (Fig. 6B). Increased fracture intensity values (e.g., > 0.4 m/m^2) cluster along and around the fold axial trace forming discontinuous patches of high intensity fracture zones along strike that are not exactly coincident with the axial trace of the anticline.

Fractures mapped in satellite imagery were assigned to one of six discrete fracture sets (A-F) based on their orientations with respect to the orientation of the interpreted fold hinge line (from Watkins et al., 2019) proximal to the interpreted fracture (see insets in Fig. 7A). Because the fold hinge exhibits some orientation variability along its length (Fig. 7A), some overlap exists between the orientations of the assigned fracture sets due to variability in the orientation of the fold hinge (Fig. 7B). Set A fractures are oriented ENE-WSW (mean strike = 59°), approximately perpendicular to the axial trace of the anticline, and typically exhibit opening mode kinematics from field-based observations. Set B fractures strike approximately parallel to the fold hinge (NNW-SSE; mean strike = 154°), and Sets C, D, E, and F are oriented approximately WNW-ESE, N-S, E-W, and NNE-SSW, with mean strikes of 111°, 178°, 086°, and 024° respectively (Fig. 7B). Fold-perpendicular (Set A) and fold-parallel (Set B) fractures make up the majority (ca. 40% and 31.5% respectively) of the total number of fractures mapped in satellite imagery. This dominance of Sets A and B accounts for the approximately bimodal orientation distribution for all combined fractures (Fig. 6A) and the overall trend for increased bulk fracture intensity towards the fold hinge. The remaining fracture sets make up 28.5% (by count) of mapped fractures from satellite imagery, with Sets C, D, E, and F representing 13%, 9%, 5.5%, and 1% of the total number of mapped fractures respectively.
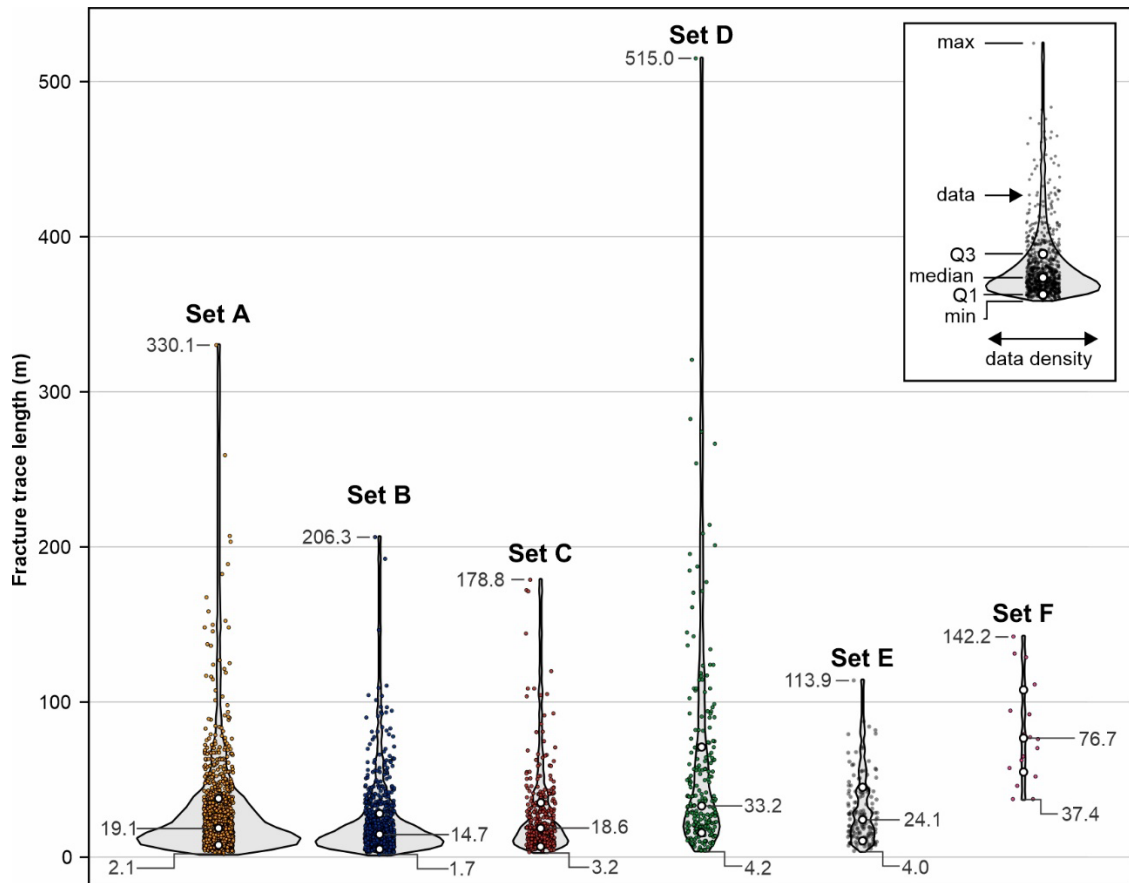
Length distribution data show that with the exception of Set F, fractures in all sets exhibit relative increases in fracture abundance at shorter length scales (see downward-widening violin plots in Fig. 8). The predominance of relatively short fractures as a proportion of the total is most pronounced in Sets A and B, as evidenced by the width of violin plots at lower length scales. Set B has the lowest minimum (1.7 m) and median (14.7 m) fracture length values and Set D (oriented N-S) contains the longest fractures, with a maximum fracture length within this set of 515 m. Note that the estimated fracture lengths in Figure 8 may overestimates because fracture segmentation not visible in lower resolution imagery (e.g., Odling, 1997).

Estimated fracture intensities for the separated fracture sets provide an overview of how fracture abundance within each set varies spatially (Fig. 9). Set A fracture intensity data show some evidence for increased intensity towards the fold hinge, but this increase is neither uniform across the fold, nor are increased intensities exactly coincident with the interpreted fold hinge position (Fig. 9A). This suggests that proximity to fold hinge only partially controls the abundance of this hinge-perpendicular fracture set. Fractures of Set B (NNW-SSE) appear to be strongly developed along the hinge of the anticline, and increases in Set B intensity appear to be closely related to the position of the fold hinge (Fig. 9B). Backlimb positions exhibit low to moderate intensities of this hinge-parallel fracture set, with only isolated patches on the backlimb showing elevated intensity values (up to 0.07 m/m^2). Sets C and D show evidence for isolated zones of increased fracture intensity but in both cases increased intensities do not appear to be systematically related to the fold hinge position (Fig. 9C, D). Fractures of Sets E and F were only identified and mapped in isolated parts of the structure. These sets show no systematic increase in

abundance at hinge/forelimb positions and therefore changes in the abundance of these fractures are not easily related to fold
315   geometry or structural position (Fig. 9E, F).

Figure 7: (A) Fracture traces separated into 6 discrete sets, based on orientations of individual fracture traces with respect to the fold hinge orientation. Rose plot in (A) shows fold hinge orientation variability along the crest of the structure, based on 15 line
320   segments of the interpreted fold hinge. Insets in (A) show along-strike variability in fold hinge and hinge-perpendicular fracture orientations. Despite this variability in absolute orientations of hinge-perpendicular fractures, these were assigned to the same fracture set (Set A). (B) Equal area, length-weighted rose plots showing orientations of interpreted fracture sets. Orientation variability and overlap between fracture set orientations is attributed to fold hinge orientation variability (see insets in A).

325

Figure 8: Violin plots showing length distributions of fractures sets interpreted from satellite imagery. Numbers refer to maximum, median, and minimum lengths for each fracture set, in meters. Fracture sets and orientations shown in Figure 7.
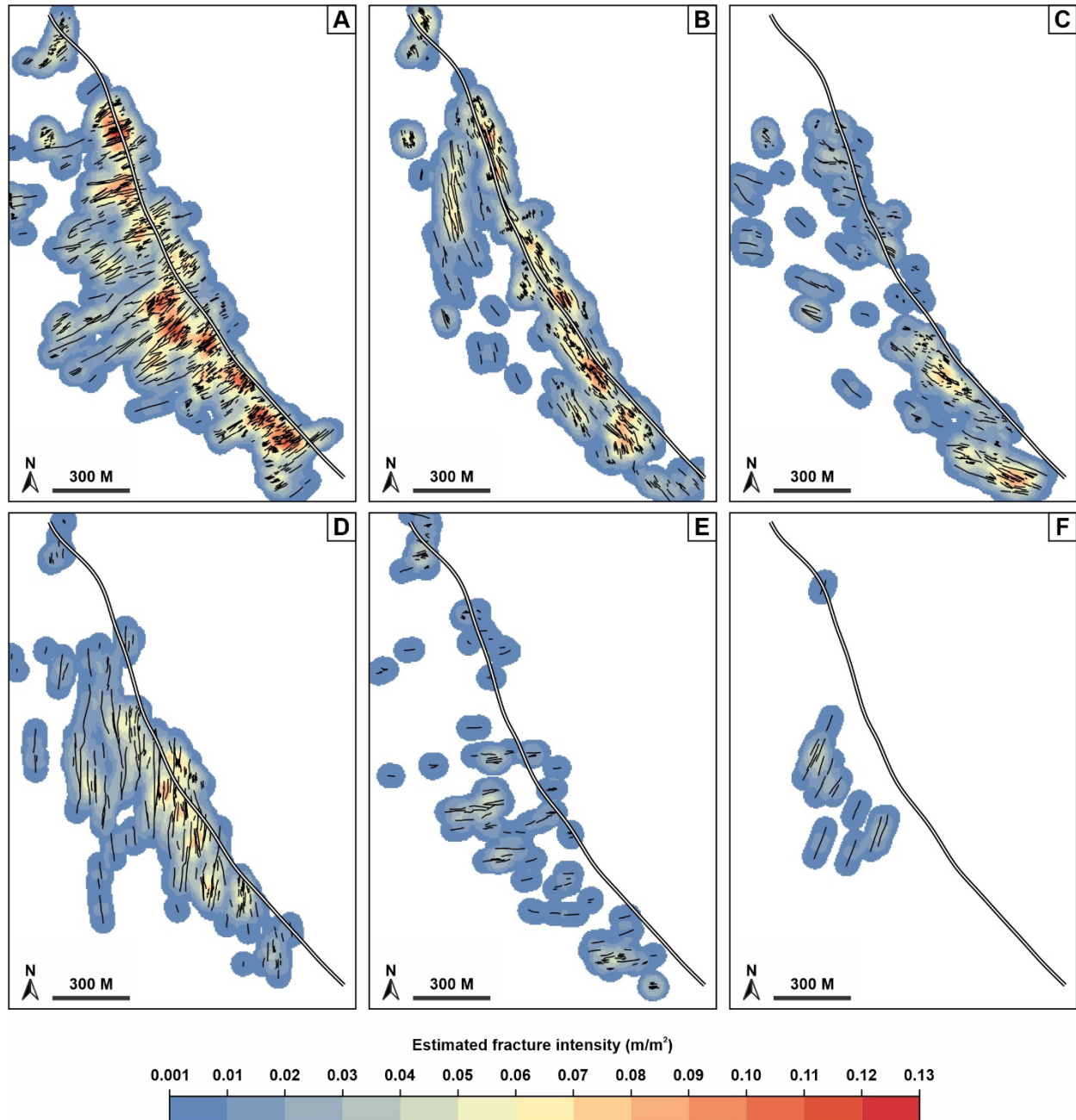
5.4 Digital outcrop analyses

Subsequent to initial mapping of fractures in satellite imagery, a second stage of fracture mapping was carried out using
330 the digital outcrop of Swift anticline. Analysis of the UAV-imagery-derived photogrammetric reconstruction (digital outcrop) focused on (i) identifying of stratigraphic exposure levels and boundaries across the crest of the structure, (ii) remapping of fracture traces at a higher resolution in order to refine the fracture map and compare results with fractures mapped from Google Earth satellite imagery, and (iii) assessing of the relationship between structural position, mapped lithologies, and fracture attributes.

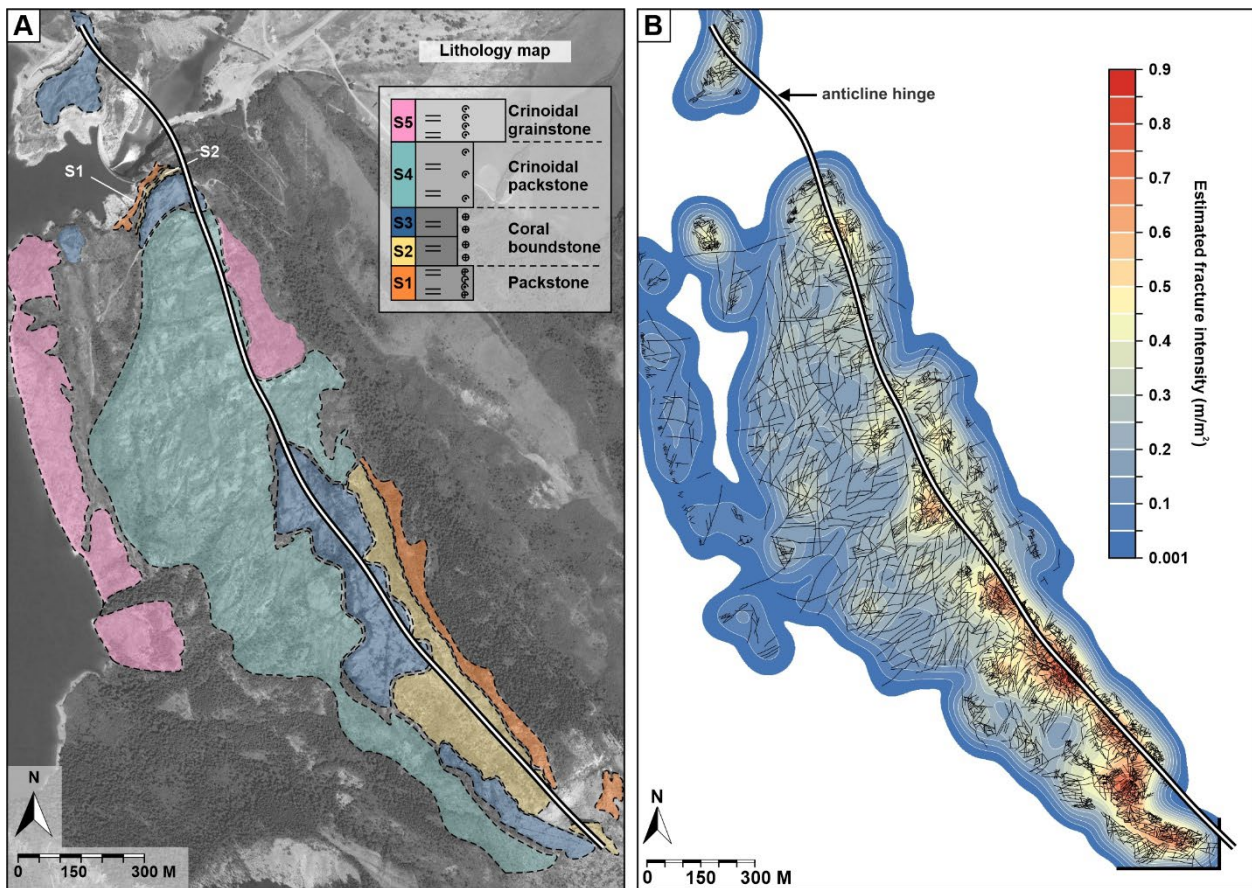335   ### 5.4.1 Digital outcrop derived lithology maps

The 3D digital outcrop allows lithological boundaries that are not clearly visible in satellite imagery (e.g., Fig. 4A) to be identified in 3D and mapped across the outcrop (see https://sketchfab.com/3d-models/swift-anticline-montana-4c60c376a2984166843fc3391b2a85b7 for low resolution, web version of the photogrammetric reconstruction). Lithological

15

boundary maps were generated by interrogating the digital outcrop in 3D and identifying lithological boundaries based on
340 variations in texture, colour, and topography across the structure.

Figure 9: (A-F) Estimated fracture intensity for fracture sets A-F. See Figure 7 for fracture set orientations. Fracture intensity
maps generated using the *Line Density* tool in *ArcMap 10.5.1* with 5 m cell sizes and 50 m search radii. Approximate position of the
345 anticline hinge shown by thick black and white line.

16

Units S1-S5, defined in physically measured stratigraphic section in the upper part of the dam cut section (Fig. 5), are exposed in fractured bedding pavements on the crest of Swift anticline and were mapped digitally, using the methodology outlined above, across the exposed parts of the structure (Fig. 10A). Unit S4 makes up the majority of the exposure surface across the crest, particularly at backlimb structural positions (Fig. 10A). Units S1, S2, S3, and S5 are discontinuously exposed across the structure, and in some cases are only sufficiently exposed for fracture mapping in a single structural position (e.g., unit S1 in forelimb position, Fig. 10A). It should be noted that lithology mapping away from the measured section at the dam was undertaken using a digital approach only, with no ground-truth data collected to confirm digital lithology mapping results. As such, the lithology map in Figure 10 likely represents an oversimplification of the exposed bedding surface map. Patches of the mapped outcrop exposure may represent thinly bedded layers between our assigned units (S1-S5) but nevertheless, our detailed digital mapping and interrogation of the digital outcrop in 3D is interpreted to have resulted in a lithology map that provides a good approximation of the lithologies exposed in the dam cut (Fig. 5) and on the crest of the structure.
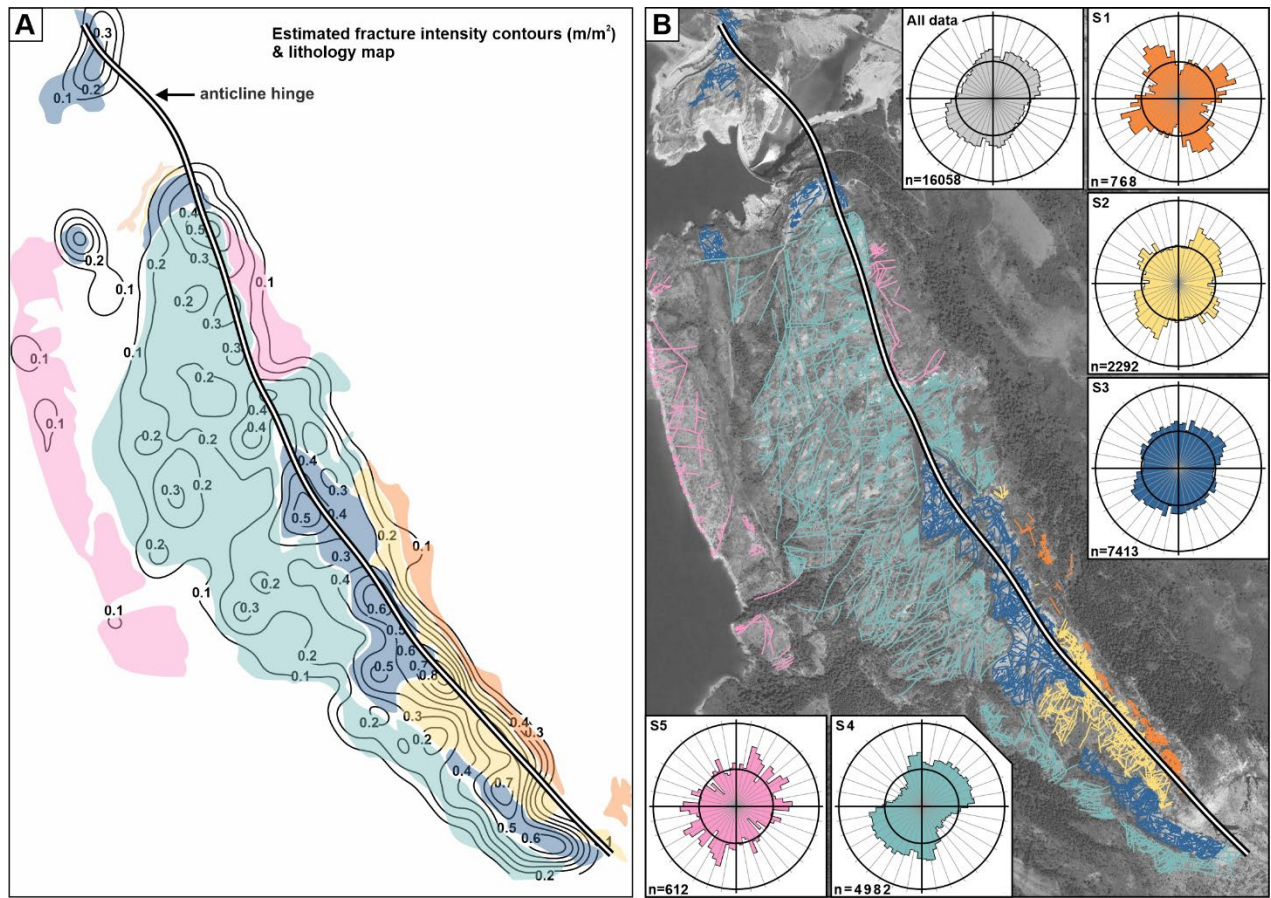

Figure 10: (A) Lithology map of Swift Anticline (see Fig. 5A, B for stratigraphic log) overlain on satellite imagery (© Google Earth/Landsat/Copernicus). Lithological mapping was performed using the digital outcrop of the anticline and projected onto satellite imagery for clarity. (B) Estimated 2D intensity (m/m²) of fractures mapped from digital outcrop (photogrammetry) data. 2D fracture intensity calculated using the *Line Density* tool in *ArcMap 10.5.1* with 5 m grid cells and 50 m sampling window radii.

5.4.2 Estimated fracture intensities from digital outcrop mapping

365   Digital mapping of fractures on the digital outcrop was performed in 3D using a medium resolution digital outcrop that covered the entire outcrop exposure at 0.24 m ground pixel resolution (compared to 0.3-0.4 m for Google Earth imagery). This second stage of fracture mapping resulted in identification and mapping of 4608 fractures (Fig. 10B), compared to 2717 fractures mapped in satellite imagery. Estimated fracture intensities for digital-outcrop-derived data are higher (up to c. 0.86 m/m^2; Fig. 10B) than for equivalent Google Earth-derived data (up to c. 0.54 m/m^2; Fig. 6B) but general trends in fracture

370   intensity for the two datasets are similar. Both intensity maps (Figs. 6B and 10B) exhibit discontinuous patches of relatively high fracture intensity around the fold hinge line, but with variations in both strike and dip directions. Neither of the fracture intensity maps show a perfect match between the position of the interpreted fold hinge position (reproduced from Watkins et al., 2019) and highest fracture intensities; in both cases the highest fracture intensities appear to be proximal to the interpreted hinge position, but a short distance (20-50 m) towards the backlimb of the structure.

375   A compiled lithology and fracture intensity map for the digital-outcrop-derived data (Fig. 11A) shows that variations in fracture intensity at Swift anticline are at least partially related to stratigraphic exposure level. There is a general trend for increased fracture intensity in the finer-grained, mud-supported units S2 and S3, as documented by fracture intensity values of 0.4 to >0.8 m/m^2 where these units are exposed. Patterns of fracture intensity contours appear to closely correspond to the mapped extents of units S2 and S3, with highest fracture intensities present towards the geographic centres of these exposed

380   units (Fig. 11A). It should be noted that there is likely an edge effect in calculated fracture intensity towards the edges of the exposure (Fig. 11) but nevertheless, units S2 and S3 exhibit the highest fracture intensities on the crest of the structure. Fracture intensity values generally decrease from unit S3 to units S4 and S5 irrespective of structural position. This is apparent where these units are exposed on the backlimb of the structure: S3, S4, and S5 are associated with fracture intensities greater than 0.4 m/m^2, greater than 0.3 m/m^2, and less than 0.2 m/m^2 respectively (Fig. 11A). Unit S4 is the only unit that is well exposed at a

385   number of structural (backlimb, hinge, and forelimb) positions. Fracture intensities in this unit increase towards the hinge of the structure (Fig. 11A), suggesting that structural position influences fracture intensity. In other units only isolated parts of the outcrop allow for comparison of fracture intensities in similar structural positions. The relative importance of structural position vs. lithological variations on fracture intensity is therefore difficult to assess but nevertheless, it appears from the data provided in Figures 10 and 11 that both of these factors play a role in observed fracture intensities at Swift anticline.

Figure 11: (A) Digital-outcrop-derived lithology map overlain onto estimated fracture intensity contours derived from the digital outcrop. (B) Digital-outcrop-derived fracture traces (n = 4608) coloured according to unit in which they were mapped, overlain on satellite imagery (© Google Earth/Landsat/Copernicus). Orientations of fracture traces by lithology shown in rose diagrams. Note, n values shown for rose plots are for fracture trace segments (i.e., straight segments between polyline nodes), rather than for entire fracture traces. Satellite imagery © Google Earth/Landsat/Copernicus.

5.4.3 Stratigraphic exposure vs. fracture orientations

Length weighted orientations for digital outcrop-derived fracture traces record a weakly preferred orientation of the fracture population of NE-SW (Fig. 11B), perpendicular to the fold hinge. This dataset records greater overall dispersion of fracture trace orientations than data derived from satellite imagery (Fig. 6A) which is indicative of greater variability in fracture orientations at smaller scales. Separation of fracture orientation data into stratigraphic units records changes in dominant fracture orientations with exposure level (Fig. 11B). Fractures traces within units S1 and S2 show dominantly bimodal distributions, with well-defined peaks in length-weighted fracture orientations that trend roughly NE-SW and NW-SE. Orientations within units S3-S5 record greater variability, with no clearly defined, dominant orientations. The approximately bimodal distributions recorded within units S1 and S2 (Fig. 11B) show the apparent dominance of hinge parallel and hinge

19

perpendicular fractures in these lithologies. Units S1 and S2 are exposed only in the hinge and forelimb zones of the structure, in which overall fracture patterns from aerial imagery show an increasing abundance of fractures oriented perpendicular and parallel to the axial trace of the fold (Fig. 9A, B). It is therefore likely that the observed changes in fracture orientations by stratigraphic exposure level (Fig. 11B) reflect structural rather than stratigraphic controls.

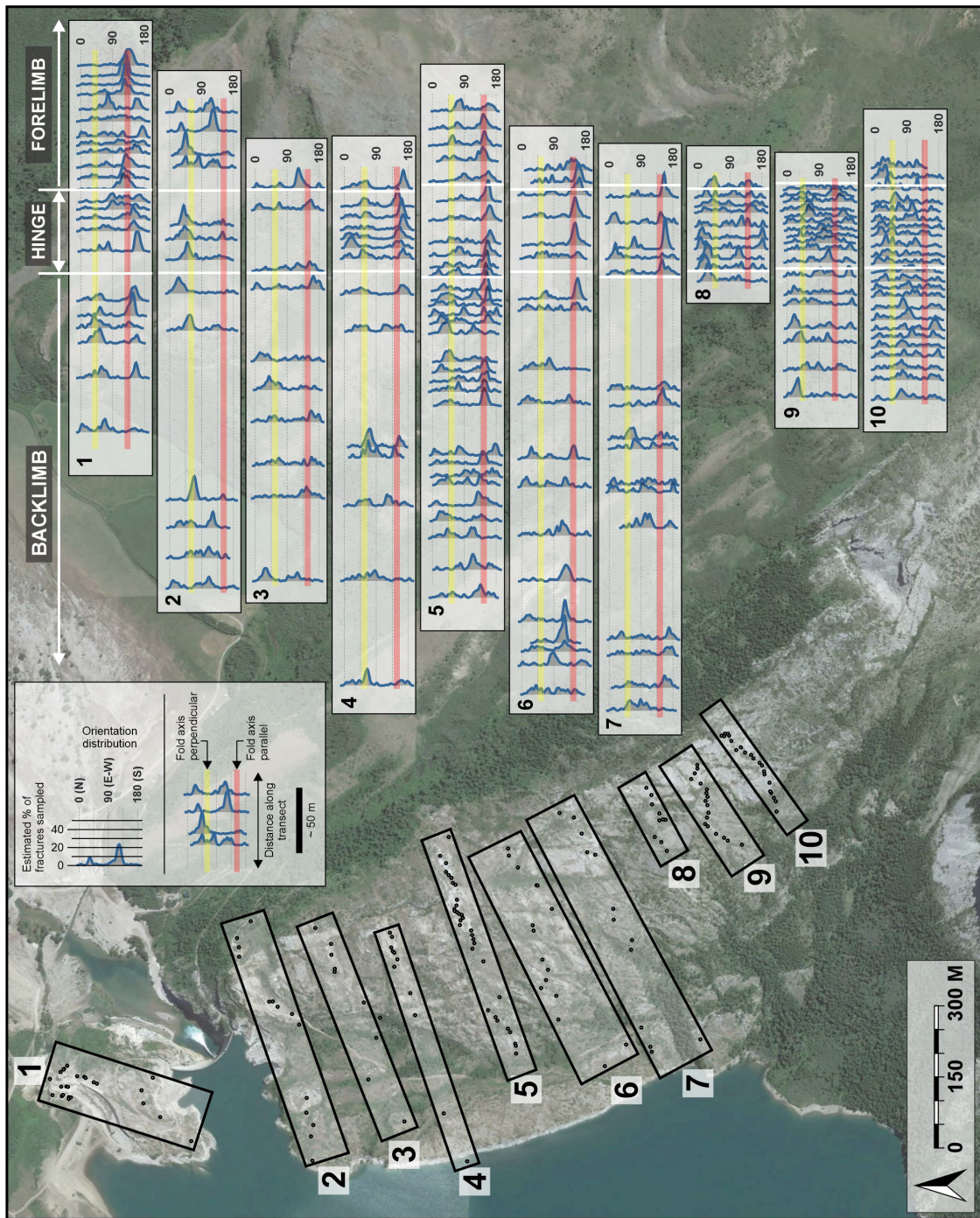## 5.5 Fracture orientations from high resolution (handheld camera) imagery

Watkins et al. (2019) assessed the influence of stratigraphic and structural factors on fracture intensity at Swift anticline. The same fracture stations as used by Watkins et al. (2019) are used here to assess fracture orientation variability in high resolution (0.2 mm pixel size) imagery.

Stacked fracture orientation histograms along a series of structural transects, derived from field-based orientation sampling, provides an overview of spatial variability in dominant fracture orientations across the structure (Fig. 12). Field data show a general trend for increased dominance of hinge-parallel fractures towards forelimb and hinge positions on the anticline. This trend is clearer in the central part of the structure (e.g., transects 3-7) where orientation histograms display distinct peaks towards SE and SSE, approximately parallel to the fold hinge axis (Fig. 12). This trend is not ubiquitous however; fracture orientations at some hinge and forelimb positions, particularly towards the southern part of the structure (e.g., transects 8, 9, 10), show no clear dominance of hinge-parallel fractures, and relatively dispersed orientations.

Strike perpendicular fractures (set B, Fig. 7B) are less prominent in field data but do show dominance in some isolated positions (e.g., backlimb, transect 1, Fig. 12). Fracture sets C, D, E and F, identified from satellite imagery (Fig. 7), are not clearly evident in field-based orientation histograms but do make up a component of dispersed fracture orientations, particularly towards the southern part of the structure. It should be noted that transects 7, 8 and 9 do not sample the forelimb of the structure, and thus the increasing dominance of hinge-parallel fractures, mapped in satellite imagery (Fig. 9), towards the forelimb of the structure may not be represented here due to a lack of exposure. Many of the ground stations, when observed in isolation, show no clearly dominant fracture orientation; general trends are only apparent when multiple histograms are stacked along structural transects.
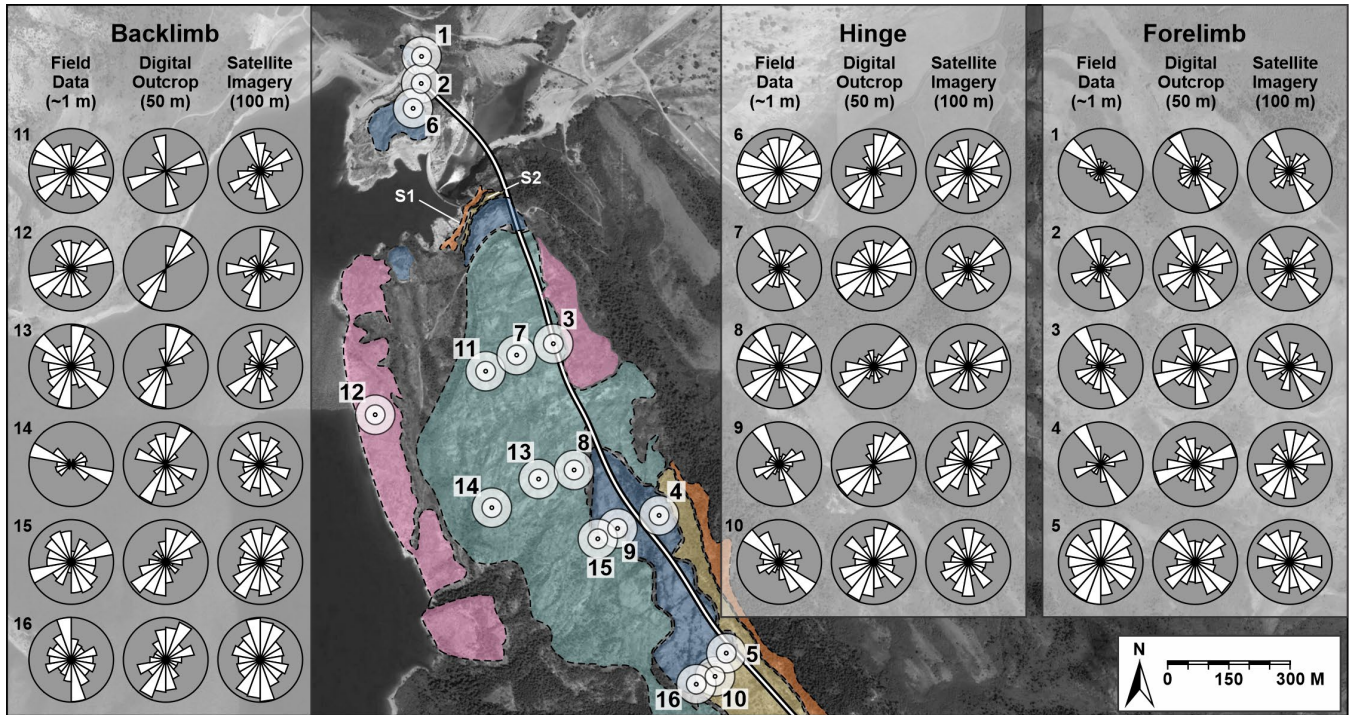
5.6 Impact of observation scale on apparent fracture orientations

To assess the impact of observation scale on apparent fracture orientations, data from ground sampling sites were compared with digital outcrop-derived (within a 50 m sampling circle) and satellite image-derived (100 m sampling window) data around field measurement stations (Fig. 13). This window sampling method allows for comparison of fracture orientations between field-based, digital outcrop, and satellite image observation scales. Fractures described in the section below are referred to according to their orientations and assigned fracture sets, as outlined in Figure 7.

Figure 12: Stacked orientation histograms, from field-based measurements, along a series of structural transects across the anticline. Interpreted structural positions are marked along upper horizontal axes of the transects. Yellow and red bars show approximate fold-perpendicular and fold-parallel orientations respectively for structural transects. Approximate orientations of yellow and red bars at each transect are derived from the interpreted fold axis in Figure 6B. Black dots and boxes on map show sample locations and data used for each transect, respectively. Satellite imagery © Google Earth/Landsat/Copernicus.

21

Field-derived orientation data generally record the dominance of hinge-parallel (set B) fractures in the forelimb and hinge of the structure (Fig. 13). Hinge-perpendicular (set A) fractures are also commonly sampled at these locations but are generally less well developed than set B. Field data from the backlimb of the structure show greater variability than in hinge-proximal positions, with no consistently dominant fracture orientations observed. In general, individual sample sites on the backlimb show greater apparent orientation dispersion (e.g., sites 11, 12, and 13) than forelimb and hinge counterparts. Marked variations in fracture orientations are also recorded at sample sites that are adjacent to each other (e.g., sites 10 and 16) towards the fold backlimb.

Figure 13: Comparison of fracture orientations at multiple observation scales. Bullseye circles on satellite image represent approximate sampling areas for field, digital outcrop, and satellite data from smallest to largest respectively. Rose plots show variation in average fracture orientation with changes in observation scale at each site. Numbers on the satellite image correspond to rows of rose plots in shaded boxes. See Figure 10 for lithology colours. Satellite imagery © Google Earth/Landsat/Copernicus.
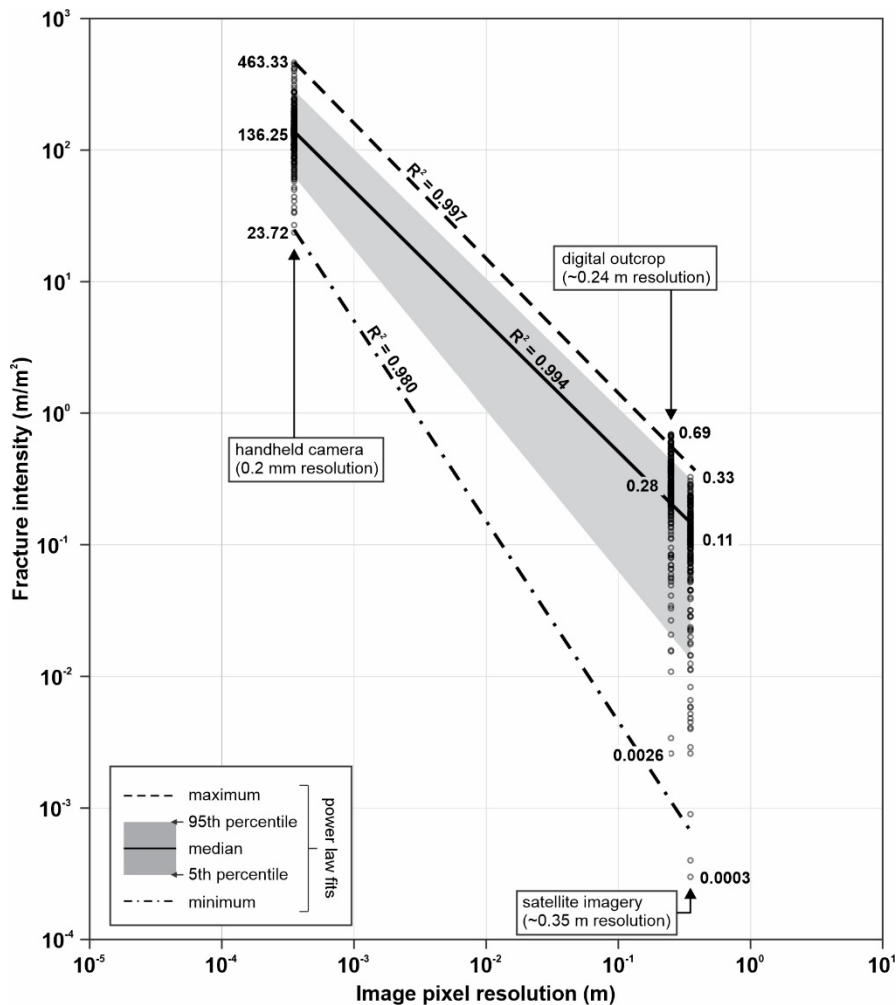
Window samples of digital outcrop and satellite image derived fracture traces show some similarity to field data at the fold forelimb (e.g., site 1; Fig. 13). Orientation distributions are generally dominated by sets A and B in forelimb digital outcrop and satellite image sampling windows, as is the case for field data (e.g., sites 1 and 2; Fig. 13). In some cases sets A and B are both recorded, but there exists a difference in fracture set dominance with observation scale. At site 2, for example, field data show the dominance of a NNW-SSE component, while digital outcrop and satellite image derived fractures within sample

22

windows around the site demonstrate an approximately bimodal orientation distribution (Fig. 13). In general, sample window data from the fold hinge and backlimb show less agreement to field data than in the forelimb and hinge of the structure. In some cases, one or more of the fracture sets is represented at all three observation scales (e.g., site 7, set A; Fig. 13), while in others, little similarity exists between datasets extracted from the same area (e.g., site 11; Fig. 13). In general, there appears to be greater agreement between observation scales where sets A and B are more strongly developed, primarily in hinge-proximal locations. General trends in fracture orientations, either from field-based sampling or by window sampling of remotely acquired data, are difficult to identify from isolated sampling of the structure due to variability in the fracture network at a range of scales.

5.7 Scaling of estimated fracture intensity

Watkins et al. (2019) employed a field-based approach to characterize fracture intensity at Swift anticline by collecting handheld imagery of fractured bedding surfaces and using the circular scanline method of Mauldon et al. (2001) to estimate fracture intensity in 193 scaled and oriented field images. The authors found that fracture intensity varies substantially at Swift anticline, and that both lithology and structural position influence fracture occurrence. Here we compare our results with those of Watkins et al. (2019) by sampling our satellite image and digital outcrop derived fracture intensity maps (Figs. 6B and 10B) at the precise sample site locations used for the previous study. Fracture intensity map sampling was performed using raster sampling tools (Extract Values to Points) in ArcMap 10.5.1.

Estimated fracture intensity varies substantially according to image pixel size and scale of observation (Fig. 14), with fracture intensity estimates of ca. 24 to 463 m/m^2 for handheld camera images (pixel size = ca. 0.2 mm), 0.0026 to 0.69 m/m^2 for digital outcrop data (pixel size = ca. 0.24 m), and 0.0003 to 0.33 m/m^2 for satellite image data (pixel size = ca. 0.35 m). Power-law regression fits for minimum, median, and maximum fracture intensity values for compiled data provide regression coefficients of 0.98 and higher, and power law exponents of 0.9 to 1.4 (Fig. 14). Although we only assess only three image pixel sizes in this analysis, the high correlation coefficients for power-law regression models suggest that prediction of fracture intensity for a given observation scale may be relatively well constrained.

Figure 14: Compilation of estimated fracture intensities and ground pixel resolutions for Swift Anticline. Fracture intensities estimated from handheld camera images are reproduced from Watkins et al. (2019).Satellite imagery and digital outcrop data generated by sampling fracture intensity rasters (Figs. 6B and 10B) using the geographic coordinates of Watkins et al. (2019) field localities. Labels denote the maximum, median, and minimum fracture intensity values for the respective datasets. Raster sampling was performed in ArcMap 10.5.1.

6 Discussion

6.1 Controls on estimated fracture intensity

We show that fracture intensity at Swift Anticline is controlled by both lithology and structural position. Digital fracture maps and associated intensity contours show that fine-grained, mud-supported wackestones are the most intensely fractured lithologies at the site (Fig. 11). Previous studies have shown that rock strength generally decreases with increasing porosity (e.g., Price, 1966; Dunn et al., 1973; Nelson, 2001) and that fine-grained, low porosity lithologies may be more brittle, and therefore more prone to intense fracturing than coarse-grained rocks (e.g., Hugman and Friedman, 1979; Wennberg et al.,

2006; Hanks et al., 2007). Our observations of increased fracture intensity in fine-grained units are in agreement with the work of Watkins et al. (2019) and others, and provides a relatively simple but logical link between rock texture and fracture intensity. Other lithological properties (e.g., bed thickness) may influence fracture abundance (e.g., McQuillan 1974; Ladeira and Price, 1981; Wennberg et al. 2006; Sun et al., 2021). Our initial analyses did not provide any strong evidence for a relationship

505 between bed thickness and fracture spacing at Swift anticline and therefore based on this early result we did not address this topic further. We did not assess mechanical layer thickness during fieldwork (from Schmidt rebound data, fracture heights etc.) and the digital outcrop analysis alone does not allow unequivocal determination of mechanical layer thickness. Future studies could focus on collecting data such as Schmidt rebound measurements, fracture heights (i.e., strata-bound vs. non-strata-bound), and observations of bed boundaries to investigate this topic further.

510 A limitation of the analysis of Watkins et al. (2019) is that specific lithologies (e.g., mud-supported units) identified in the field could not be easily correlated across the exposed crest of the structure. By digitally mapping lithological boundaries across the structure in 3D (Fig. 10A), spatial variations in fracture properties can be directly tied to stratigraphic exposure levels and therefore larger-scale, three-dimensional assessments of fracture intensity vs. stratigraphic exposure can be more easily performed using the digital approach (e.g., Corradetti et al., 2018; Triantafyllou et al., 2019). It should be noted that

515 limits to image resolution may partly hamper lithologic boundary mapping (e.g., Humair et al., 2015) and while every effort was made to generate robust interpretations in this study, we acknowledge that delineating precise boundaries between units was not always straightforward. A potential solution to this problem, resources allowing, would be to carry out initial digital mapping or reconnaissance of sites using satellite imagery or photogrammetric reconstructions, followed by field campaigns focused on further data collection and field-checking of digital interpretations (e.g., Scheiber et al., 2015).

520 We provide evidence for increased fracture abundances towards the hinge zone of the anticline (Figs. 6 and 10). These results are generally consistent with the results of Watkins et al. (2019) but in both this and the previous study the relationship between structural position and fracture intensity is not straightforward (e.g., Fig. 6 in Watkins et al., 2019). We show that fracture intensity values generally increase towards the fold hinge but that the zones of highest fracture intensities are not always perfectly coincident with the interpreted hinge position (Fig. 6B and 10B). Increased fracture abundances in hinge-

525 proximal zones have been recorded on folds in a multitude of settings (e.g., Ramsay, 1967; Hanks et al., 1997; Hennings et al., 2000; Wennberg et al., 2007; Ghosh and Mitra, 2009; Watkins et al. 2015) but, as noted above, lithology also influences estimated fracture intensity at Swift Anticline. Because multiple stratigraphic units are exposed on the crest of the structure, our fracture intensity maps (Figs. 6B and 10B) record the influence of both structural position and stratigraphic exposure level on fracture abundance. Where multiple lithologies are exposed on fold structures, it should perhaps be expected that apparent

530 fracture intensity does not directly correlate with either structural position (e.g., forelimb vs. backlimb) or proximity to the fold hinge.

6.2 Fracture orientation variability

Natural fracture orientations at Swift Anticline are highly variable and appear to vary according to stratigraphic exposure level (Fig. 11), structural position (Figs. 9 and 12), and observation scale (Fig. 13). We do, however, document at least two systematic fracture sets that appear to conform to established models of fold-related fracturing. Most of the Set A (fold-axis-perpendicular) and Set B (fold-axis-parallel) fractures observed on the crest of the anticline (Figs. 7 and 8) are interpreted as being fold related. These sets exhibit (i) a general increase in intensity towards the interpreted fold hinge position, and (ii) orientations that are consistently parallel (Set B) and perpendicular (Set A) to the local fold hinge orientation (Fig. 7A). Opening-mode fractures oriented parallel and perpendicular to fold hinges have been documented on contractional anticlines in a number of settings (e.g., McQuillan, 1974; Bergbauer & Pollard, 2004; Cooper et al., 2006; Wennberg et al., 2006; Francioni et al., 2019), including at sites proximal to Swift Anticline in the Sawtooth Range (e.g., Stearns, 1964; Ghosh & Mitra, 2009).

We interpret the hinge-parallel (Set B) fractures at Swift Anticline as opening mode fractures formed in response to outer arc bending of relatively competent carbonate strata during fold formation, consistent with predicted bending strain on contractional folds (e.g., Ramsay, 1967). While most fractures observed at the site show no evidence for displacement parallel to the fracture walls (i.e., shear), the cross-section exposure of the anticline (Fig. 5B) exposes several thrusts and back-thrusts with similar strike orientations to fracture set B (Figs. 5C and 7). It is therefore possible that a small proportion of the Set B fractures observed in map view (Fig. 7) are reverse faults rather than bending-related opening-mode fractures. The underlying mechanisms that led to the development of Set A fractures is somewhat speculative. The hinge-perpendicular (Set A) fractures observed in the field typically exhibit opening mode kinematics and these may have developed as a result of extension parallel to the fold hinge. Subtle along-strike plunge variations of the fold and associated hinge-parallel curvature (e.g., Cosgrove and Ameen, 2000) may be a potential mechanism for this hinge-parallel extension. We did not find any clear relationship between hinge-parallel curvature and hinge-perpendicular fracture intensity at the site, however, because of difficulties in accurately estimating fold curvature from the vegetated, eroded fold crest.

Fracture Sets C, D, E, and F exhibit no clear relationship between fracture intensity and proximity to the fold hinge (Fig. 9) and are less consistently oriented with respect to the fold hinge compared to Sets A and B (Fig. 7). From these general patterns, we tentatively interpret Sets C, D, E, and F as having developed prior to, or possibly after, fold formation. The units exposed on the crest of Swift Anticline were deposited during the Mississippian (Nichols, 1984), and based on tectonic frameworks for North America in many published sources (e.g., Marshak et al., 2000; Weil and Yonkee, 2023), these rocks likely experienced variable regional stress through time related to multiple Late Paleozoic through Paleogene convergent tectonic events in western North America, although only the late Cretaceous to Palaeocene development of the Sawtooth Range (Fuentes et al., 2012) resulted in any significant contractional shortening. The strata exposed at the site have also experienced documented localized forebulge-related extension during the Middle Jurassic (Ward and Sears, 2007), and probably regional extension (eastern Basin and Range province) during the Cenozoic (e.g., Wallace et al., 1990; Stewart et al., 1998).

565   The units exposed at Swift Anticline have therefore experienced at least two phases of prolonged regional contraction, one phase of localized extension, and one phase of regional, plate-scale extension. Because of this complex tectonic evolution and the likely variations in principal stress orientations, fracture failure modes, and fracture orientations that this deformation history implies (Ferrill et al., 2021), it should perhaps be expected that multiple fracture sets (with shear, compaction, or opening failure modes) could have developed both before and after fold formation at the site. Candidate structures include

570   conjugate strike-slip faults that may have formed during early contraction and layer-parallel shortening, prior to fold formation (Tavani et al., 2015; Ferrill et al., 2015). Sets C, E, and F orientations are approximately consistent with the expected range of orientations for strike-slip faults related to ENE-directed contraction but without definitive evidence for strike-slip faulting (e.g., from kinematic indicators), this remains speculative. While we did not observe kinematic indicators consistent with strike-slip faulting, our efforts here focus on fracture characterization using remote sensing data, rather than on detailed field

575   observations.

       The existence of pre-folding fractures could have resulted in the reactivation of optimally oriented fracture sets to accommodate strain during folding, that may not directly conform to the expected orientation in conceptual models (e.g., Tavani et al., 2015). A further consideration is the curvilinear nature of the fold hinge line and the implications for strain and fracture set development, as compared to the models derived for linear folds. Future studies focused on detailed field

580   observations, microscopy, and dating of fracture cements would likely provide valuable insights into fracture kinematics and timing at the site.

6.3 Predicting fracture intensities and orientations

       Fracture orientations derived from field images, digital outcrop data, and satellite imagery show a general trend for increased proportions of hinge-parallel and hinge-perpendicular fractures towards the anticline hinge and forelimb. In contrast,

585   more dispersed and less predictable orientations are present towards the backlimb of the structure (Fig. 13). This overall pattern results in a more clearly defined structural grain in the hinge and forelimb, and as such, greater agreement between observation scales at these structural positions. Less systematic or dispersed fracture orientations on the backlimb results in greater disparity in orientations between observation scales, and a general trend for disagreement between data derived from field images, digital outcrop data, and satellite imagery (Fig. 15). These results suggest that extrapolation or prediction of fracture

590   orientations from one observation scale to another is not straightforward, and that the scaling of fracture properties is dependent on both structural position and deformation history, among other factors.

       Our observations of a more clearly defined structural grain in hinge and forelimb positions are similar to those of Watkins et al. (2015, 2018), who showed that in strata that have experienced a long and complex deformation history, fracture orientations are more consistent and predictable at hinge and forelimb positions, and generally unpredictable on backlimbs.

595   Recent subsurface image log analysis by Wang et al. (2023) provides evidence for more clustered but lower intensity fracture patterns in the backlimb of the East Painter Reservoir anticline (also in the Rockies) than in hinge and forelimb positions. This result is potentially compatible with the patterns observed at Swift anticline. Our conceptual model of fold-related fracturing

acknowledges that complex fracture patterns are likely to exist in rocks that have experienced complex deformation histories, and that fold-related fracturing is more likely to overprint pre-existing deformation fabrics in hinge and forelimb positions

600 (Fig. 15). Further, we account for stratigraphic exposure level, based on our observation that fine-grained, thinly bedded units at the site exhibit higher fracture intensity than coarse-grained, thickly bedded units (Fig. 15). This model develops early conceptual models that predict highly organized, discrete fracture sets with little orientation variability by (i) accounting for the effects of lithological properties on fracture abundance, (ii) acknowledging that brittle deformation fabrics may form before, during, and after folding, and (iii) documenting that the scaling of fracture properties is likely dependent on structural
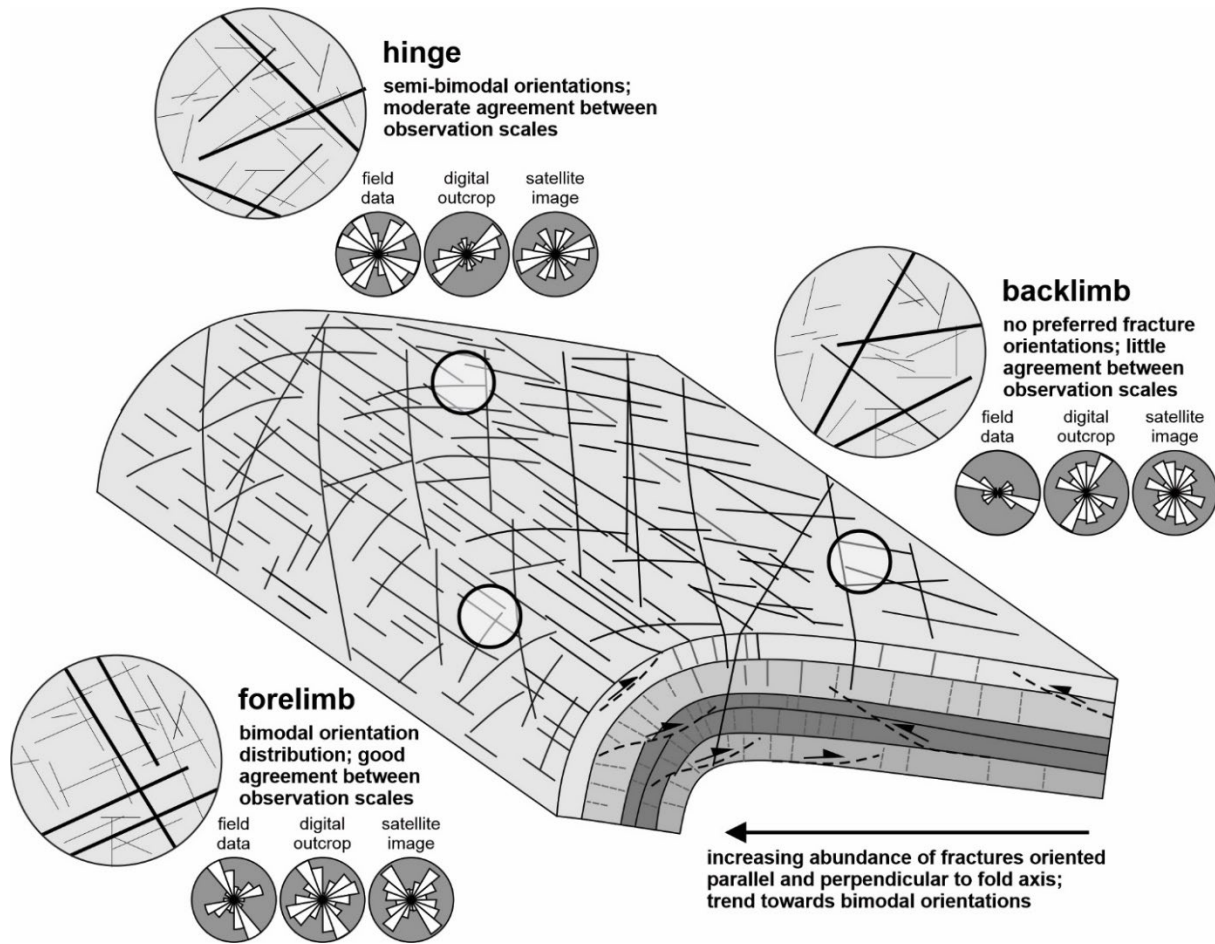
605 position.

Figure 15: Conceptual diagram showing variations in fracture attributes at Swift Anticline. Results from this study provide evidence for three general trends in fracture attributes: (i) increasing intensity of hinge-parallel and hinge-perpendicular fractures
610 **towards the fold hinge which results in a bulk increase in fracture intensity in hinge-proximal positions, (ii) higher fracture intensities in fine-grained, thinly-bedded units, (iii) variable fracture orientations in backlimb positions, with little agreement between observation scales, (iv) moderate to high intensity of hinge-parallel and hinge-perpendicular fractures and some agreement between fracture orientation measurements at hinge positions, and (v) moderate to high intensity of hinge-parallel and hinge-perpendicular fractures and good agreement between fracture orientation measurements in high, medium, and low**
615 **resolution data towards the forelimb. Rose diagrams are a subset of data provided in Fig. 13.**

Our results and conceptual model suggest that accurate prediction of fracture properties requires analysis not only of lithologic and structural properties, but also of fracture property scaling, and the spatial variability of scaling relationships. Finally, predictions should account for all known deformation events and the effects that these events may have on existing fracture patterns present-day.

620

7 Conclusions

In this study we assess the effects of structural position, lithology, and variable data resolution on estimates of natural fracture network properties. By characterizing fracture intensities and orientations derived from mapping fractures at three image resolutions, we assess how interacting geological factors influence fracture development and the scaling of natural fracture systems. Our findings are relevant for estimating and extrapolating fracture properties in the subsurface, where data resolution and coverage are limited. The key findings of this study are:

625

1. Hinge-parallel and hinge-perpendicular fractures exhibit systematic increases in abundance towards the fold hinge at Swift anticline. In contrast, fractures not oriented parallel or perpendicular to the fold hinge show no systematic variations in abundance across the structure.

630

2. We document a general trend for increased fracture intensity in relatively fine-grained, thinly bedded units at the site. Variations in stratigraphic exposure level across the crest of the structure result in fracture intensity maps that capture both lithologic and structural elements. We attribute mismatches between zones of highest fracture intensity and the fold hinge position to variations in rock type, with finer-grained units exhibiting higher fracture intensities than coarse-grained units in equivalent structural positions.

635

3. Fracture orientations at the site are highly variable, and only hinge-parallel and hinge-perpendicular fractures are consistently oriented with respect to the orientation of the fold hinge. Further, these fracture sets are consistently identified at all observational scales in the forelimb and hinge; and show increased intensity in these regions. Other fracture sets show less consistency between observational scales and no intensity relationship with fold position.

4. Fracture orientation data exhibit greatest agreement between observation scales at hinge and forelimb positions where the hinge-parallel and hinge-perpendicular fracture sets are best developed. Based on these results, we suggest that the scaling of fracture properties is likely to be dependent on structural position. Extrapolation of fracture properties from one scale to another should therefore account for variations in deformation intensity.

640

Author contributions

All authors performed data collection during the field work. AC collected UAV imagery and processed photogrammetry data. Fracture mapping and data analysis was performed by AC. The draft manuscript and figures were prepared by AC and finalized

645

after input and edits were provided by co-authors. Manuscript conceptualization by AC with input from co-authors through numerous discussions.

Competing interests

The authors declare that they have no conflicts of interest.

650 ## Code/Data availability

Data are provided in the manuscript and will be uploaded as supplemental information in the final version.

Acknowledgements

References

Agosta, F., Alessandroni, M., Antonellini, M., Tondi, E. and Giorgioni, M., 2010. From fractures to flow: a field-based 660 quantitative analysis of an outcropping carbonate reservoir. Tectonophysics, 490(3-4), 197-213.

Aliverti, E., Biron, M., Francesconi, A., Mattiello, D., Nardon, S. and Peduzzi, C., 2003. Data analysis, processing and 3D fracture network simulation at wellbore scale for fractured reservoir description. Geological Society, London, Special Publications, 209(1), 27-37.

Awdal, A., Healy, D. and Alsop, G.I., 2016. Fracture patterns and petrophysical properties of carbonates undergoing regional 665 folding: A case study from Kurdistan, N Iraq. Marine and Petroleum Geology, 71, 149-167.

Bachu, S., 1995. Synthesis and model of formation-water flow, Alberta Basin, Canada. AAPG Bulletin, 79(8), 1159-1178.

Becker, I., Koehrer, B., Waldvogel, M., Jelinek, W. and Hilgers, C., 2018. Comparing fracture statistics from outcrop and reservoir data using conventional manual and t-LiDAR derived scanlines in Ca2 carbonates from the Southern Permian Basin, Germany. Marine and Petroleum Geology, 95, 228-245.

670 Bemis, S.P., Micklethwaite, S., Turner, D., James, M.R., Akciz, S., Thiele, S.T. and Bangash, H.A., 2014. Ground-based and UAV-Based photogrammetry: A multi-scale, high-resolution mapping tool for structural geology and paleoseismology. Journal of Structural Geology, 69, 163-178.

Bergbauer, S. and Pollard, D.D., 2004. A new conceptual fold-fracture model including prefolding joints, based on the Emigrant Gap anticline, Wyoming. Geological Society of America Bulletin, 116(3-4), 294-307.

675 Bödvarsson, G.S. and Tsang, C.F., 1982. Injection and thermal breakthrough in fractured geothermal reservoirs. Journal of Geophysical Research: Solid Earth, 87(B2), 1031-1048.

Bond, C.E., Wightman, R. and Ringrose, P.S., 2013. The influence of fracture anisotropy on CO2 flow. Geophysical Research Letters, 40(7), 1284-1289.

Bond, C.E., Kremer, Y., Johnson, G., Hicks, N., Lister, R., Jones, D.G., Haszeldine, R.S., Saunders, I., Gilfillan, S.M., Shipton, Z.K. and Pearce, J., 2017. The physical characteristics of a CO2 seeping fault: The implications of fracture permeability for carbon capture and storage integrity. International Journal of Greenhouse Gas Control, 61, 49-60.

Bonnet, E., Bour, O., Odling, N.E., Davy, P., Main, I., Cowie, P. and Berkowitz, B., 2001. Scaling of fracture systems in geological media. Reviews of geophysics, 39(3), 347-383.

Bossennec, C., Frey, M., Seib, L., Bär, K. and Sass, I., 2021. Multiscale characterisation of fracture patterns of a crystalline reservoir analogue. Geosciences, 11(9), 371.

Bowness, N.P., Cawood, A.J., Ferrill, D.A., Smart, K.J. and Bellow, H.B., 2022. Mineralogy controls fracture containment in mechanically layered carbonates. Geological Magazine, 1-19.

Burberry, C.M., Cannon, D.L., Cosgrove, J.W. and Engelder, T., 2019. Fracture patterns associated with the evolution of the Teton anticline, Sawtooth Range, Montana, USA. Geological Society, London, Special Publications, 487(1), 229-261.

Caine, J.S., Evans, J.P. and Forster, C.B., 1996. Fault zone architecture and permeability structure. Geology, 24(11), 1025-1028.

Casini, G., Gillespie, P.A., Vergés, J., Romaire, I., Fernández, N., Casciello, E., Saura, E., Mehl, C., Homke, S., Embry, J.C. and Aghajari, L., 2011. Sub-seismic fractures in foreland fold and thrust belts: insight from the Lurestan Province, Zagros Mountains, Iran. Petroleum Geoscience, 17(3), 263-282.

Castaing, C., Halawani, M.A., Gervais, F., Chilès, J.P., Genter, A., Bourgine, B., Ouillon, G., Brosse, J.M., Martin, P., Genna, A. and Janjou, D., 1996. Scaling relationships in intraplate fracture systems related to Red Sea rifting. Tectonophysics, 261(4), 291-314.

Cawood, A.J., Bond, C.E., Howell, J.A., Butler, R.W. and Totake, Y., 2017. LiDAR, UAV or compass-clinometer? Accuracy, coverage and the effects on structural models. Journal of Structural Geology, 98, 67-82.

Cawood, A.J., Corradetti, A., Granado, P. and Tavani, S., 2022. Detailed structural analysis of digital outcrops: A learning example from the Kermanshah-Qulqula radiolarite basin, Zagros Belt, Iran. Journal of Structural Geology, 154, 104489.

Chabani, A., Trullenque, G., Ledésert, B.A. and Klee, J., 2021. Multiscale Characterization of fracture patterns: A case study of the Noble Hills Range (Death Valley, CA, USA), application to geothermal reservoirs. Geosciences, 11(7), 280.

Cooke, M.L. and Underwood, C.A., 2001. Fracture termination and step-over at bedding interfaces due to frictional slip and interface opening. Journal of Structural Geology, 23(2-3), 223-238.

Cooke, M.L., Simo, J.A., Underwood, C.A. and Rijken, P., 2006. Mechanical stratigraphic controls on fracture patterns within carbonates and implications for groundwater flow. Sedimentary Geology, 184(3-4), 225-239.

Cooper, M.A. 1991. The analysis of fracture systems in subsurface thrust structures from the Foothills of the Canadian Rockies. In; Thrust Tectonics, McClay, K.R (ed), Chapman & Hall, London, 391-406.

Cooper, S.P., Goodwin, L.B. and Lorenz, J.C., 2006. Fracture and fault patterns associated with basement-cored anticlines: The example of Teapot Dome, Wyoming. AAPG Bulletin, 90(12), 1903-1920.

Corradetti, A., Tavani, S., Parente, M., Iannace, A., Vinci, F., Pirmez, C., Torrieri, S., Giorgioni, M., Pignalosa, A. and Mazzoli, S., 2018. Distribution and arrest of vertical through-going joints in a seismic-scale carbonate platform exposure (Sorrento peninsula, Italy): insights from integrating field survey and digital outcrop model. Journal of Structural Geology, 108, 121-136.

Cosgrove, J.W. and Ameen, M.S., 1999. A comparison of the geometry, spatial organization and fracture patterns associated with forced folds and buckle folds. Geological Society, London, Special Publications, 169(1), 7-21.

31

De Marsily, G., Delay, F., Gonçalvès, J., Renard, P., Teles, V. and Violette, S., 2005. Dealing with spatial heterogeneity. Hydrogeology Journal, 13(1), 161-183.

720 Dimmen, V., Rotevatn, A. and Lecomte, I., 2023. Imaging of small-scale faults in seismic reflection data: Insights from seismic modelling of faults in outcrop. Marine and Petroleum Geology, 147, 105980.

Dunn, D.E., LaFountain, L.J. and Jackson, R.E., 1973. Porosity dependence and mechanism of brittle fracture in sandstones. Journal of Geophysical Research, 78(14), 2403-2417.

Ferrill, D.A., Winterle, J., Wittmeyer, G., Sims, D.W., Colton, S., Armstrong, A., Morris, A.P., 1999. Stressed rock strains
725 groundwater at Yucca Mountain, Nevada. Geological Society of America Today 9, 1–8.

Ferrill, D.A., Smart, K.J., Cawood, A.J. and Morris, A.P., 2021. The fold-thrust belt stress cycle: Superposition of normal, strike-slip, and thrust faulting deformation regimes. Journal of Structural Geology, 148, 104362.

Fischer, M.P. and Wilkerson, M.S., 2000. Predicting the orientation of joints from fold shape: Results of pseudo–three-dimensional modeling and curvature analysis. Geology, 28(1), 15-18.

730 Fox, D.B., Sutter, D., Beckers, K.F., Lukawski, M.Z., Koch, D.L., Anderson, B.J. and Tester, J.W., 2013. Sustainable heat farming: Modeling extraction and recovery in discretely fractured geothermal reservoirs. Geothermics, 46, 42-54.

Francioni, M., Pace, P., Vitulli, M., Sciarra, N. and Calamita, F.,2019. Distribution of joints in the hinge-line culmination of foreland-verging overturned anticlines: an example from the Montagna dei Fiori structure in the Central Apennines of Italy. Geological Magazine, 156(8), 1445–1454.

735 Fuentes, F., DeCelles, P.G. and Constenius, K.N., 2012. Regional structure and kinematic history of the Cordilleran fold-thrust belt in northwestern Montana, USA. Geosphere, 8(5), 1104-1128.

Gautschi, A., 2001. Hydrogeology of a fractured shale (Opalinus Clay): Implications for deep geological disposal of radioactive wastes. Hydrogeology Journal, 9(1), 97-107.

Gholami, R., Raza, A. and Iglauer, S., 2021. Leakage risk assessment of a CO2 storage site: A review. Earth-Science Reviews,
740 223, 103849.

Ghosh, K. and Mitra, S., 2009. Structural controls of fracture orientations, intensity, and connectivity, Teton anticline, Sawtooth Range, Montana. AAPG Bulletin, 93(8), 995-1014.

Gillespie, P.A., Howard, C.B., Walsh, J.J. and Watterson, J., 1993. Measurement and characterisation of spatial distributions of fractures. Tectonophysics, 226(1-4),.113-141.

745 Gillespie, P.A., Walsh, J.J., Watterson, J., Bonson, C.G. and Manzocchi, T., 2001. Scaling relationships of joint and vein arrays from The Burren, Co. Clare, Ireland. Journal of Structural Geology, 23(2-3), 183-201.

Glaas, C., Vidal, J. and Genter, A., 2021. Structural characterization of naturally fractured geothermal reservoirs in the central Upper Rhine Graben. Journal of Structural Geology, 148, 104370.

Gong, L., Wang, J., Gao, S., Fu, X., Liu, B., Miao, F., Zhou, X. and Meng, Q., 2021. Characterization, controlling factors and
750 evolution of fracture effectiveness in shale oil reservoirs. Journal of Petroleum Science and Engineering, 203, 108655.

Green, A.G. and Mair, J.A., 1983. Subhorizontal fractures in a granitic pluton: Their detection and implications for radioactive waste disposal. Geophysics, 48(11), 1428-1449.

Hancock, P.L., 1985. Brittle microtectonics: principles and practice. Journal of Structural Geology, 7(3-4), 437-457.

Hanks, C.L., Lorenz, J., Teufel, L. and Krumhardt, A.P., 1997. Lithologic and structural controls on natural fracture
755 distribution and behavior within the Lisburne Group, northeastern Brooks Range and North Slope subsurface, Alaska. AAPG bulletin, 81(10), 1700-1720.

Hardebol, N.J., Maier, C., Nick, H., Geiger, S., Bertotti, G. and Boro, H., 2015. Multiscale fracture network characterization and impact on flow: A case study on the Latemar carbonate platform. Journal of Geophysical Research: Solid Earth, 120(12), 8197-8222.

760 Harris, J.F., Taylor, G.L. and Walper, J.L., 1960. Relation of deformational fractures in sedimentary rocks to regional and local structure. AAPG Bulletin, 44(12), 1853-1873.

Healy, D., Rizzo, R.E., Cornwell, D.G., Farrell, N.J., Watkins, H., Timms, N.E., Gomez-Rivas, E. and Smith, M., 2017. FracPaQ: A MATLAB™ toolbox for the quantification of fracture patterns. Journal of Structural Geology, 95, 1-16.

Hennings, P.H., Olson, J.E. & Thompson, L.B. 2000. Combining outcrop data and three-dimensional structural models to
765   characterise fractured reservoirs: an example from Wyoming. AAPG Bulletin, 84, 830–849

Holl, J.E. & Anastasio, D.J. 1992. Deformation of a foreland carbonate thrust system, Sawtooth Range, Montana. Geological Society of America Bulletin, 104, 994–953.

Hooker, J.N., Laubach, S.E. and Marrett, R., 2013. Fracture-aperture size—Frequency, spatial distribution, and growth processes in strata-bounded and non-strata-bounded fractures, Cambrian Mesón Group, NW Argentina. Journal of
770   Structural Geology, 54, 54-71.

Hugman, R.H.H. & Friedman, M. 1979. Effects of texture and composition on mechanical behaviour of experimentally deformed carbonate rocks. AAPG Bulletin, 63, 1478–1489.

Humair, F., Abellan, A., Carrea, D., Matasci, B., Epard, J.L. and Jaboyedoff, M., 2015. Geological layers detection and characterisation using high resolution 3D point clouds: example of a box-fold in the Swiss Jura Mountains. European
775   Journal of Remote Sensing, 48(1), 541-568.

Iding, M. and Ringrose, P., 2010. Evaluating the impact of fractures on the performance of the In Salah CO_2 storage site. International Journal of Greenhouse Gas Control, 4(2), 242-248.

Inks, T.L., Engelder, T., Jenner, E., Golob, B., Hocum, J.S. and O'Brien, D.G., 2015. Marcellus fracture characterization using P-wave azimuthal velocity attributes: Comparison with production and outcrop data. Interpretation, 3(3), SU1-SU15.

780 Ishii, E., 2022. Constant-head step injection tests to quantify the stress dependence of fracture transmissivity in an excavation damaged zone: A case study from the Horonobe Underground Research Laboratory. International Journal of Rock Mechanics and Mining Sciences, 159, 105229.

James, M.R. and Robson, S., 2012. Straightforward reconstruction of 3D surfaces and topography with a camera: Accuracy and geoscience application. Journal of Geophysical Research: Earth Surface, 117(F3).

785 Kou, Z., Wang, T., Chen, Z. and Jiang, J., 2021. A fast and reliable methodology to evaluate maximum CO_2 storage capacity of depleted coal seams: A case study. Energy, 231, 120992.

Ladeira, F.L. and Price, N.J., 1981. Relationship between fracture spacing and bed thickness. Journal of Structural Geology, 3(2), 179-183.

Laubach, S.E., Olson, J.E. and Gross, M.R., 2009. Mechanical and fracture stratigraphy. AAPG Bulletin, 93(11),1413-1426.

790 Laubach, S.E., Lander, R.H., Criscenti, L.J., Anovitz, L.M., Urai, J.L., Pollyea, R.M., Hooker, J.N., Narr, W., Evans, M.A., Kerisit, S.N. and Olson, J.E., 2019. The role of chemistry in fracture pattern development and opportunities to advance interpretations of geological materials. Reviews of Geophysics, 57(3), 1065-1111.

Li, L. and Lee, S.H., 2008. Efficient field-scale simulation of black oil in a naturally fractured reservoir through discrete fracture networks and homogenized media. SPE Reservoir evaluation & engineering, 11(04), 750-758.

795 Lisle, R.J. 1992. Constant bed-length folding: three-dimensional geometrical implications. Journal of Structural Geology, 14, 245–252.

Lisle, R.J. 1994. Detection of zones of abnormal strains in structures using Gaussian curvature analysis. AAPG Bulletin, 78, 1811–1819.

Ma, J., Vaszi, A.Z., Couples, G.D. and Harris, S.D., 2007. The link between a heterogeneous model and its flow response: examples from fault damage zones highlighting issues in domain discretization and flow simulation. Geological Society, London, Special Publications, 292(1), 337-352.

Mäkel, G.H., 2007. The modelling of fractured reservoirs: Constraints and potential for fracture network geometry and hydraulics analysis. Geological Society, London, Special Publications, 292(1), 375-403.

Marrett, R. and Allmendinger, R.W., 1992. Amount of extension on" small" faults: An example from the Viking graben. Geology, 20(1), 47-50.

Marshak, S., Karlstrom, K. and Timmons, J.M., 2000. Inversion of Proterozoic extensional faults: An explanation for the pattern of Laramide and Ancestral Rockies intracratonic deformation, United States. Geology, 28(8), 735-738.

Mauldon, M., Dunne, W.M. & Rohrbaugh, M.B., Jr., 2001. Circular Scanlines and circular windows: new tools for characterizing the geometry of fracture traces. Journal of Structural Geology, 23, 247–258.

McGinnis, R.N., Ferrill, D.A., Smart, K.J., Morris, A.P., Higuera-Diaz, C. and Prawica, D., 2015. Pitfalls of using entrenched fracture relationships: Fractures in bedded carbonates of the Hidden Valley Fault Zone, Canyon Lake Gorge, Comal County, Texas. AAPG Bulletin, 99(12), 2221-2245.

McGinnis, R.N., Ferrill, D.A., Morris, A.P., Smart, K.J. and Lehrmann, D., 2017. Mechanical stratigraphic controls on natural fracture spacing and penetration. Journal of Structural Geology, 95, 160-170.

McQuillan, H. 1973. Small-scale fracture density in Asmari Formation of Southwest Iran and its relation to bed thickness and structural setting. AAPG Bulletin, 57, 2367–2385.

McQuillan, H., 1974. Fracture patterns on Kuh-e Asmari anticline, southwest Iran. AAPG Bulletin, 58(2), 236-246.

Medici, G., Smeraglia, L., Torabi, A. and Botter, C., 2021. Review of modeling approaches to groundwater flow in deformed carbonate aquifers. Groundwater, 59(3), 334-351.

Mitra, S. 1986. Duplex structures and imbricate thrust systems: geometry, structural position, and hydrocarbon potential. AAPG Bulletin, 70, 1087–1112.

Moore, J.P. and Walsh, J.J., 2021. Quantitative analysis of Cenozoic faults and fractures and their impact on groundwater flow in the bedrock aquifers of Ireland. Hydrogeology Journal, 29(8), 2613-2632.

Morris, A.P., Ferrill, D.A., Sims, D.W., Franklin, N. and Waiting, D.J., 2004. Patterns of fault displacement and strain at Yucca Mountain, Nevada. Journal of Structural Geology, 26(9), 1707-1725.

Mudge, M.R. 1982. A résumé of the structural geology of the Northern Disturbed Belt, northwest Montana. Geological Studies of the Cordilleran Thrust Belt, 1, 91–122.

Nadimi, S., Forbes, B., Moore, J., Podgorney, R. and McLennan, J.D., 2020. Utah FORGE: Hydrogeothermal modeling of a granitic based discrete fracture network. Geothermics, 87, 101853.

Narr, W. and Suppe, J., 1991. Joint spacing in sedimentary rocks. Journal of Structural Geology, 13(9), 1037-1048.

Nelson, R., 2001. Geologic analysis of naturally fractured reservoirs. Elsevier.

Nichols, K.M. 1984. Stratigraphy of the upper part of the Madison Group, Sawtooth Range, northwestern Montana. Montana Geological Society, 1984 Field Conference, Northwestern Montana, I27-I4A.

Nichols, K.M. 1986. Regional Significance of Lithologic Correlation of Mississippian Rocks at Pentagon Mountain and the Sawtooth Range, Northwestern Montana. USGS Open-File Report 86-39 (one Plate).

Odling, N.E., 1997. Scaling and connectivity of joint systems in sandstones from western Norway. Journal of Structural Geology, 19(10), 1257-1271.

Price, N. J., Fault and Joint Development in Brittle and Semi-Brittle Rock, Pergamon, New York, 1966

Ramsay, J.G., 1967. Folding and fracturing of rocks. Mc Graw Hill Book Company, 568 p.

840 Rawnsley, K.D., Rives, T., Petti, J.P., Hencher, S.R. and Lumsden, A.C., 1992. Joint development in perturbed stress fields near faults. Journal of Structural Geology, 14(8-9), 939-951.

Rawnsley, K., De Keijzer, M., Wei, L., Bettembourg, S., Asyee, W., Massaferro, J.L., Swaby, P., Drysdale, D. and Boettcher, D., 2007. Characterizing fracture and matrix heterogeneities in folded Devonian carbonate thrust sheets, Waterton tight gas fields, Western Canada. Geological Society, London, Special Publications, 270(1), 265-279.

845 Scheiber, T., Fredin, O., Viola, G., Jarna, A., Gasser, D. and Łapińska-Viola, R., 2015. Manual extraction of bedrock lineaments from high-resolution LiDAR data: methodological bias and human perception. Gff, 137(4), 362-372.

Seers, T.D. and Hodgetts, D., 2014. Comparison of digital outcrop and conventional data collection approaches for the characterization of naturally fractured reservoir analogues. Geological Society, London, Special Publications, 374(1), 51-77.

850 Shaik, A.R., Rahman, S.S., Tran, N.H. and Tran, T., 2011. Numerical simulation of fluid-rock coupling heat transfer in naturally fractured geothermal system. Applied thermal engineering, 31(10), 1600-1606.

Sinclair, S., 1980, Analysis of macroscopic fractures on Teton anticline, northwestern Montana: M.S. thesis, Texas A&M University, College Station, Texas, 102 p.

Singdahlsen, D. S., 1986. Structural geology of the Swift Reservoir Culmination, Sawtooth Range, Montana. MSc Thesis, 855 Montana State University, Bozeman, Montana, 124 p., 2 plates.

Smeraglia, L., Mercuri, M., Tavani, S., Pignalosa, A., Kettermann, M., Billi, A. and Carminati, E., 2021. 3D Discrete Fracture Network (DFN) models of damage zone fluid corridors within a reservoir-scale normal fault in carbonates: multiscale approach using field data and UAV imagery. Marine and Petroleum Geology, 126, 104902.

Spence, G.H., Couples, G.D., Bevan, T.G., Aguilera, R., Cosgrove, J.W., Daniel, J.M. and Redfern, J., 2014. Advances in the 860 study of naturally fractured hydrocarbon reservoirs: a broad integrated interdisciplinary applied topic. Geological Society, London, Special Publications, 374(1), 1-22.

Spooner, J. A., 1984, Field and laboratory study of fracture characteristics as a function of bed curvature in folded dolomites, Sawtooth Mountains, Montana: M.S. thesis, University of Oklahoma, Norman, Oklahoma, 135 p.

Stearns, D.W. 1964. Macrofracture patterns on Teton Anticline, northwest Montana. Transactions of the American 865 Geophysical Union, 45, 107-108

Stearns, D.W., 1969. Fracture as a mechanism of flow in naturally deformed layered rocks. In Proceedings of the Conference on Research in Tectonics, Kink Bands and Brittle Deformation. Geological Survey of Canada, Papers 68(52), 79-96.

Stearns, D.W. & Friedman, M. 1972. Reservoirs in fractured rock: Geologic exploration methods. In: King, R.E. (ed.) Stratigraphic Oil and Gas Fields: Classification, Exploration Methods, and Case Histories. AAPG Memoirs, 16, 82–106.

870 Streltsova, T.D., 1976. Hydrodynamics of groundwater flow in a fractured formation. Water resources research, 12(3), 405-414.

Strijker, G., Bertotti, G. and Luthi, S.M., 2012. Multi-scale fracture network analysis from an outcrop analogue: A case study from the Cambro-Ordovician clastic succession in Petra, Jordan. Marine and Petroleum Geology, 38(1), 104-116.

Stewart, J.H., Anderson, R.E., Aranda-Gómez, J.J., Beard, L.S., Billingsley, G.H., Cather, S.M., Dilles, J.H., Dokka, R.K., 875 Faulds, J.E., Ferrari, L., Grose, T.L. Map showing Cenozoic tilt domains and associated structural features, western North

America. Accommodation zones and transfer zones: The regional segmentation of the Basin and Range province: Geological Society of America Special Paper 323(1).

Sun, J., Gamboa, E.S., Schechter, D. and Rui, Z., 2016. An integrated workflow for characterization and simulation of complex fracture networks utilizing microseismic and horizontal core data. Journal of Natural Gas Science and Engineering, 34, 1347-1360.

Sun, X., Gomez-Rivas, E., Alcalde, J., Martín-Martín, J.D., Ma, C., Muñoz-López, D., Cruset, D., Cantarero, I., Griera, A. and Travé, A., 2021. Fracture distribution in a folded fluvial succession: the Puig-reig anticline (South-eastern Pyrenees). Marine and Petroleum Geology, 132, 105169.

Tamagawa, T. and Pollard, D.D., 2008. Fracture permeability created by perturbed stress fields around active faults in a fractured basement reservoir. AAPG Bulletin, 92(6), 743-764.

Tavani, S., Storti, F., Lacombe, O., Corradetti, A., Muñoz, J.A. and Mazzoli, S., 2015. A review of deformation pattern templates in foreland basin systems and fold-and-thrust belts: Implications for the state of stress in the frontal regions of thrust wedges. Earth-Science Reviews, 141, 82-104.

Thomas, L.K., Dixon, T.N. and Pierson, R.G., 1983. Fractured reservoir simulation. Society of Petroleum Engineers Journal, 23(01), 42-54.

Triantafyllou, A., Watlet, A., Le Mouélic, S., Camelbeeck, T., Civet, F., Kaufmann, O., Quinif, Y. and Vandycke, S., 2019. 3-D digital outcrop model for analysis of brittle deformation and lithological mapping (Lorette cave, Belgium). Journal of Structural Geology, 120, 55-66.

Ukar, E., Laubach, S.E. and Hooker, J.N., 2019. Outcrops as guides to subsurface natural fractures: Example from the Nikanassin Formation tight-gas sandstone, Grande Cache, Alberta foothills, Canada. Marine and Petroleum Geology, 103, 255-275.

Vollgger, S.A. and Cruden, A.R., 2016. Mapping folds and fractures in basement and cover rocks using UAV photogrammetry, Cape Liptrap and Cape Paterson, Victoria, Australia. Journal of Structural Geology, 85, 168-187.

Wallace, C.A., Lidke, D.J. and Schmidt, R.G., 1990. Faults of the central part of the Lewis and Clark line and fragmentation of the Late Cretaceous foreland basin in west-central Montana. Geological Society of America Bulletin, 102(8), 1021-1037.

Wang, Q., Narr, W. and Laubach, S.E., 2023. Quantitative characterization of fracture spatial arrangement and intensity in a reservoir anticline using horizontal wellbore image logs and an outcrop analogue. Marine and Petroleum Geology, 152, 106238.

Ward, E.G. and Sears, J.W., 2007. Reinterpretation of fractures at Swift Reservoir, Rocky Mountain thrust front, Montana: Passage of a Jurassic forebulge?. Geological Society of America Special Papers, 433, 197-210.

Watanabe, K. and Takahashi, H., 1995. Fractal geometry characterization of geothermal reservoir fracture networks. Journal of Geophysical Research: Solid Earth, 100(B1), 521-528.

Watkins, H., Butler, R.W., Bond, C.E. and Healy, D., 2015. Influence of structural position on fracture networks in the Torridon Group, Achnashellach fold and thrust belt, NW Scotland. Journal of Structural Geology, 74, 64-80.

Watkins, H., Healy, D., Bond, C.E. and Butler, R.W., 2018. Implications of heterogeneous fracture distribution on reservoir quality; an analogue from the Torridon Group sandstone, Moine Thrust Belt, NW Scotland. Journal of Structural Geology, 108, 180-197.

Watkins, H., Bond, C.E., Cawood, A.J., Cooper, M.A. and Warren, M.J., 2019. Fracture distribution on the Swift Reservoir Anticline, Montana: Implications for structural and lithological controls on fracture intensity. Geological Society, London, Special Publications, 487(1), 209-228.

Weil, A.B. and Yonkee, A., 2023. The Laramide orogeny: Current understanding of the structural style, timing, and spatial distribution of the classic foreland thick-skinned tectonic system. In: Laurentia: Turning Points in the Evolution of a Continent, Geological Society of America Memoirs 220,

920 Wennberg, O.P., Svånå, T., Azizzadeh, M., Aqrawi, A.M.M., Brockbank, P., Lyslo, K.B. and Ogilvie, S., 2006. Fracture intensity vs. mechanical stratigraphy in platform top carbonates: the Aquitanian of the Asmari Formation, Khaviz Anticline, Zagros, SW Iran. Petroleum Geoscience, 12(3), 235-246.

Wennberg, O.P., Azizzadeh, M., Aqrawi, A.A.M., Blanc, E., Brockbank, P., Lyslo, K.B., Pickard, N., Salem, L.D. and Svånå, T., 2007. The Khaviz Anticline: an outcrop analogue to giant fractured Asmari Formation reservoirs in SW Iran. In:
925 Lonergan, L., Jolly, R.J.H., Rawnsley, K. & Sanderson, D.J. (eds) Fractured Reservoirs. Geological Society, London, Special Publications, 270, 23–42.

Worthington, M.H. and Lubbe, R., 2007. The scaling of fracture compliance. Geological Society, London, Special Publications, 270(1), 73-82.

Wu, H. and Pollard, D.D., 1995. An experimental study of the relationship between joint spacing and layer thickness. Journal
930 of Structural Geology, 17(6), 887-905.

Yielding, G., Needham, T. and Jones, H., 1996. Sampling of fault populations using sub-surface data: a review. Journal of Structural Geology, 18(2-3), 135-146.

Yin, T. and Chen, Q., 2020. Simulation-based investigation on the accuracy of discrete fracture network (DFN) representation. Computers and Geotechnics, 121, 103487.

935 Yu, H., Lu, C., Chen, W. and Li, H., 2021. Permeability changes in fractured Tamusu mudstone in the context of radioactive waste disposal. Bulletin of Engineering Geology and the Environment, 80(10), 7945-7957.